

# CO<sub>2</sub> infrared emission as a diagnostic of planet-forming regions of disks

Arthur D. Bosman<sup>1</sup>, Simon Bruderer<sup>2</sup>, and Ewine F. van Dishoeck<sup>1,2</sup>

<sup>1</sup> Leiden Observatory, Leiden University, PO Box 9513, 2300 RA Leiden, The Netherlands  
e-mail: bosman@strw.leidenuniv.nl

<sup>2</sup> Max-Planck-Institut für Extraterrestrische Physik, Gießenbachstrasse 1, 85748 Garching, Germany

Received 24 October 2016 / Accepted 23 January 2017

## ABSTRACT

**Context.** The infrared ro-vibrational emission lines from organic molecules in the inner regions of protoplanetary disks are unique probes of the physical and chemical structure of planet-forming regions and the processes that shape them. These observed lines are mostly interpreted with local thermal equilibrium (LTE) slab models at a single temperature.

**Aims.** We aim to study the non-LTE excitation effects of carbon dioxide (CO<sub>2</sub>) in a full disk model to evaluate: (i) what the emitting regions of the different CO<sub>2</sub> ro-vibrational bands are; (ii) how the CO<sub>2</sub> abundance can be best traced using CO<sub>2</sub> ro-vibrational lines using future JWST data and; (iii) what the excitation and abundances tell us about the inner disk physics and chemistry. CO<sub>2</sub> is a major ice component and its abundance can potentially test models with migrating icy pebbles across the iceline.

**Methods.** A full non-LTE CO<sub>2</sub> excitation model has been built starting from experimental and theoretical molecular data. The characteristics of the model are tested using non-LTE slab models. Subsequently the CO<sub>2</sub> line formation was modelled using a two-dimensional disk model representative of T Tauri disks where CO<sub>2</sub> is detected in the mid-infrared by the *Spitzer* Space Telescope.

**Results.** The CO<sub>2</sub> gas that emits in the 15  $\mu\text{m}$  and 4.5  $\mu\text{m}$  regions of the spectrum is not in LTE and arises in the upper layers of disks, pumped by infrared radiation. The  $\nu_2$  15  $\mu\text{m}$  feature is dominated by optically thick emission for most of the models that fit the observations and increases linearly with source luminosity. Its narrowness compared with that of other molecules stems from a combination of the low rotational excitation temperature ( $\sim 250$  K) and the inherently narrower feature for CO<sub>2</sub>. The inferred CO<sub>2</sub> abundances derived for observed disks range from  $3 \times 10^{-9}$  to  $1 \times 10^{-7}$  with respect to total gas density for typical gas/dust ratios of 1000, similar to earlier LTE disk estimates. Line-to-continuum ratios are low, in the order of a few percent, stressing the need for high signal-to-noise ( $S/N > 300$ ) observations for individual line detections.

**Conclusions.** The inferred CO<sub>2</sub> abundances are much lower than those found in interstellar ices ( $\sim 10^{-5}$ ), indicating a reset of the chemistry by high temperature reactions in the inner disk. JWST-MIRI with its higher spectral resolving power will allow a much more accurate retrieval of abundances from individual *P*- and *R*-branch lines, together with the <sup>13</sup>CO<sub>2</sub> *Q*-branch at 15  $\mu\text{m}$ . The <sup>13</sup>CO<sub>2</sub> *Q*-branch is particularly sensitive to possible enhancements of CO<sub>2</sub> due to sublimation of migrating icy pebbles at the iceline(s). Prospects for JWST-NIRSpec are discussed as well.

**Key words.** protoplanetary disks – molecular processes – astrochemistry – radiative transfer – line: formation

## 1. Introduction

Most observed exo-planets orbit close to their parent star (for a review see: [Udry & Santos 2007](#); [Winn & Fabrycky 2015](#)). The atmospheres of these close-in planets show a large diversity in molecular composition ([Madhusudhan et al. 2014](#)). This diversity in molecular composition must be set during planet formation and thus be representative of the natal protoplanetary disk. Understanding the chemistry of the inner, planet-forming regions of circumstellar disks around young stars will thus give us another important piece of the puzzle of planet formation. Prime molecules for such studies are H<sub>2</sub>O, CO, CO<sub>2</sub> and CH<sub>4</sub> which are the major oxygen- and carbon-bearing species that set the overall C/O ratio ([Öberg et al. 2011](#)).

The chemistry in the inner disk, that is, its inner few AU, differs from that in the outer disk. It lies within the H<sub>2</sub>O and CO<sub>2</sub> icelines so all icy planetesimals are sublimated. The large range of temperatures (100–1500 K) and densities ( $10^{10}$ – $10^{16}$  cm<sup>-3</sup>) then makes for a diverse chemistry across the inner disk region (see e.g. [Willacy et al. 1998](#); [Markwick et al. 2002](#); [Agúndez et al. 2008](#); [Henning & Semenov 2013](#); [Walsh et al. 2015](#)). The

driving cause for this diversity is high temperature chemistry: some molecules such as H<sub>2</sub>O and HCN have reaction barriers in their formation pathways that make it difficult to produce the molecule in high abundances at temperatures below a few hundred Kelvin. As soon as the temperature is high enough to overcome these barriers, formation is fast and these molecules become major reservoirs of oxygen and nitrogen. An interesting example is formed by the main oxygen bearing molecules, H<sub>2</sub>O and CO<sub>2</sub>: the gas phase formation of both these molecules includes the OH radical. At temperatures below  $\sim 200$  K the formation of CO<sub>2</sub> is faster, leading to high gas phase abundances, up to  $\sim 10^{-6}$  with respect to (w.r.t.) total gas density, in regions where CO<sub>2</sub> is not frozen out. When the temperature is high enough, H<sub>2</sub>O formation will push most of the gas phase oxygen into H<sub>2</sub>O and the CO<sub>2</sub> abundance drops to  $\sim 10^{-8}$  ([Agúndez et al. 2008](#); [Walsh et al. 2014, 2015](#)). Such chemical transitions can have strong implications for the atmospheric content of gas giants formed in these regions if most of their atmosphere is accreted from the surrounding gas.

A major question is to what extent the inner disk abundances indeed reflect high temperature chemistry or whether

continuously migrating and sublimating icy planetesimals and pebbles at the icelines replenish the disk atmospheres (Stevenson & Lunine 1988; Ciesla & Cuzzi 2006). Interstellar ices are known to be rich in CO<sub>2</sub>, with typical abundances of 25% w.r.t. H<sub>2</sub>O ice, or about 10<sup>-5</sup> w.r.t. total gas density (de Graauw et al. 1996; Gibb et al. 2004; Bergin et al. 2005; Pontoppidan et al. 2008; Boogert et al. 2015). Cometary ices show similarly high CO<sub>2</sub>/H<sub>2</sub>O abundance ratios (Mumma & Charnley 2011; Le Roy et al. 2015). Of all molecules with high ice abundances, CO<sub>2</sub> shows the largest contrast between interstellar ice and high temperature chemistry abundances, and could therefore be a good diagnostic of its chemistry. Pontoppidan & Blevins (2014) argue based on *Spitzer* Space Telescope data that CO<sub>2</sub> is not inherited from the interstellar medium but is reset by chemistry in the inner disk. However, that analysis used a local thermodynamic equilibrium (LTE) CO<sub>2</sub> excitation model coupled with a disk model and did not investigate the potential of future instruments, which could be more sensitive to a contribution from sublimating planetesimals. Here we re-consider the retrieval of CO<sub>2</sub> abundances in the inner regions of protoplanetary disks using a full non-LTE excitation and radiative transfer disk model, with a forward look to the new opportunities offered by the *James Webb* Space Telescope (JWST).

The detection of infrared vibrational bands seen from CO<sub>2</sub>, C<sub>2</sub>H<sub>2</sub> and HCN, together with high energy rotational lines of OH and H<sub>2</sub>O, was one of the major discoveries of the *Spitzer* Space Telescope (e.g. Lahuis et al. 2006; Carr & Najita 2008, 2011; Salyk et al. 2008, 2011b; Pascucci et al. 2009, 2013; Pontoppidan et al. 2010; Najita et al. 2011). These data cover wavelengths in the 10–35 μm range at low spectral resolving power of  $\lambda/\Delta\lambda = 600$ . Complementary ground-based infrared spectroscopy of molecules such as CO, OH, H<sub>2</sub>O, CH<sub>4</sub>, C<sub>2</sub>H<sub>2</sub> and HCN also exists at shorter wavelengths in the 3–5 μm range (e.g. Najita et al. 2003; Gibb et al. 2007; Salyk et al. 2008, 2011a; Fedele et al. 2011; Mandell et al. 2012; Gibb & Horne 2013; Brown et al. 2013). The high spectral resolving power of  $R = 25\,000\text{--}10^5$  for instruments like Keck/NIRSPEC and VLT/CRIRES have resolved the line profiles and have revealed interesting kinematical phenomena, such as disk winds in the inner disk regions (Pontoppidan et al. 2008, 2011; Bast et al. 2011; Brown et al. 2013). Further advances are expected with VLT/CRIRES+ as well as through modelling of current data with more detailed physical models.

Protoplanetary disks have a complex physical structure (see Armitage 2011, for a review) and putting all physics, from magnetically induced turbulence to full radiative transfer, into a single model is not feasible. This means that simplifications must be made. During the *Spitzer* era, the models used to explain the observations were usually LTE excitation slab models at a single temperature. With 2D physical models such as RADLITE (Pontoppidan et al. 2009) and with full 2D physical-chemical models such as Dust and Lines (DALI, Bruderer et al. 2012; Bruderer 2013) or Protoplanetary Disk Model (ProDiMo, Woitke et al. 2009) it is now possible to fully take into account the large range of temperatures and densities as well as the non-local excitation effects. For example, it has been shown that it is important to include radiative pumping introduced by hot (500–1500 K) thermal dust emission of regions just behind the inner rim. This has been done for H<sub>2</sub>O by Meijerink et al. (2009) who concluded that to explain the mid-infrared water lines observed with *Spitzer*, water is located in the inner ~1 AU in a region where the local gas-to-dust ratio is 1–2 orders of magnitude higher than the interstellar medium (ISM) value. Antonellini et al. (2015, 2016) performed a protoplanetary disk

parameter study to see how disk parameters affect the H<sub>2</sub>O emission. Mandell et al. (2012) compared an LTE disk model analysis using RADLITE with slab models and concluded that, while inferred abundance ratios were similar with factors of a few, there could be orders of magnitude differences in absolute abundances depending on the assumed emitting area in slab models (see also discussion in Salyk et al. 2011b). Thi et al. (2013) concluded that the CO infrared emission from disks around Herbig stars was rotationally cool and vibrationally hot due to a combination of infrared and ultraviolet (UV) pumping fields (see also Brown et al. 2013). Bruderer et al. (2015) modelled the non-LTE excitation and emission of HCN concluding that the emitting area for mid-infrared lines can be ten times larger in disks than the assumed emitting area in slab models due to infrared pumping. Our study of CO<sub>2</sub> is along similar lines as that for HCN.

As CO<sub>2</sub> cannot be observed through rotational transitions in the far-infrared and submillimeter, because of the lack of a permanent dipole moment, it must be observed through its vibrational transitions at near- and mid-infrared wavelengths. The CO<sub>2</sub> in our own atmosphere makes it impossible to detect these CO<sub>2</sub> lines from astronomical sources from the ground, and even at altitudes of 13 km with SOFIA. This means that CO<sub>2</sub> has to be observed from space. CO<sub>2</sub> has been observed by *Spitzer* in protoplanetary disks through its  $v_2$   $Q$ -branch at 15 μm where many individual  $Q$ -band lines combine into a single broad  $Q$ -branch feature at low spectral resolution (Lahuis et al. 2006; Carr & Najita 2008). These gaseous CO<sub>2</sub> lines have first been detected in high mass protostars and shocks with the Infrared Space Observatory (ISO, e.g. van Dishoeck et al. 1996; Boonman et al. 2003a,b). CO<sub>2</sub> also has a strong band around 4.3 μm due to the  $v_3$  asymmetric stretch mode. This mode has high Einstein  $A$  coefficients and thus should thus be easily observable, but has not been seen from CO<sub>2</sub> gas towards protoplanetary disks or protostars, in contrast with the corresponding feature in CO<sub>2</sub> ice (van Dishoeck et al. 1996).

The CO<sub>2</sub>  $v_2$   $Q$ -branch profile is slightly narrower than that of C<sub>2</sub>H<sub>2</sub> and HCN observed at similar wavelengths. These results suggest that CO<sub>2</sub> is absent (or strongly under-represented) in the inner, hottest regions of the disk. Full disk LTE modelling of RNO 90 by Pontoppidan & Blevins (2014) using RADLITE showed that the observations of this disk favour a low CO<sub>2</sub> abundance (10<sup>-4</sup> w.r.t. H<sub>2</sub>O, ≈10<sup>-8</sup> w.r.t. total gas density). The slab models by Salyk et al. (2011b) indicate smaller differences between the CO<sub>2</sub> and H<sub>2</sub>O abundances, although CO<sub>2</sub> is still found to be 2 to 3 orders of magnitude lower in abundance.

To properly analyse CO<sub>2</sub> emission from disks, a full non-LTE excitation model of the CO<sub>2</sub> ro-vibrational levels must be made, using molecular data from experiments and detailed quantum calculations. This model can then be used to perform a simple slab model study to see under which conditions non-LTE effects may be important. These same slab model tests are also used to check the influences of the assumptions made in setting up the ro-vibrational excitation model. Such CO<sub>2</sub> models have been developed in the past for evolved asymptotic giant branch stars (e.g. Cami et al. 2000; González-Alfonso & Cernicharo 1999) and shocks (e.g. Boonman et al. 2003b), but not applied to disks.

Our CO<sub>2</sub> excitation model is coupled with a full protoplanetary disk model computed with DALI to investigate the importance of non-LTE excitation, infrared pumping and dust opacity on the emission spectra. In addition, the effects of varying some key disk parameters such as source luminosity and gas/dust ratios on line fluxes and line-to-continuum ratios are investigated. Finally, *Spitzer* data for a set of T Tauri disks are analysed to

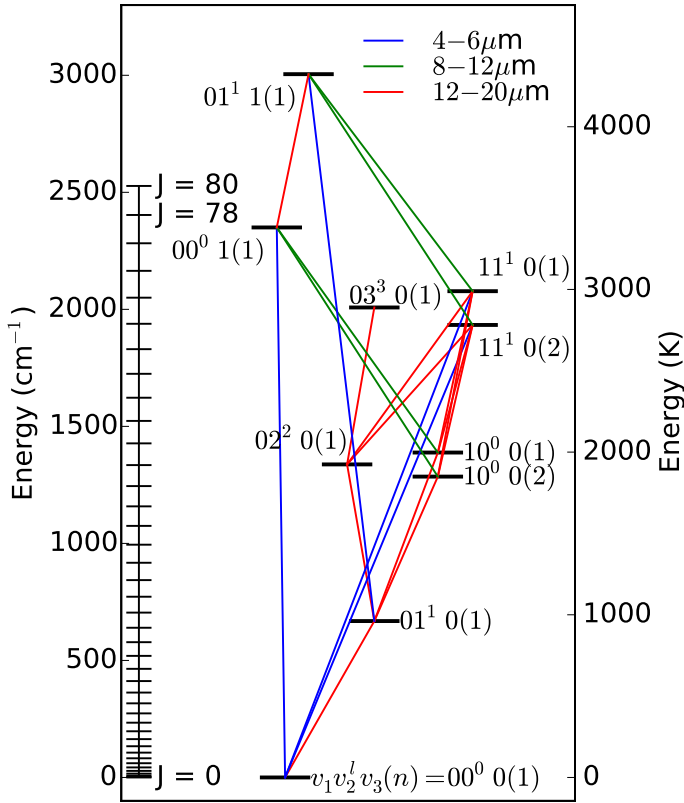


**Fig. 1.** Vibrational energy levels of the CO<sub>2</sub> molecule (right) together with the rotational ladder of the ground state (left). We note that for the ground state the rotational ladder increases with  $\Delta J = 2$ . Lines connecting the vibrational levels denote the strongest absorption and emission pathways. The colour indicates the wavelength range of the transition: blue, 4–6  $\mu\text{m}$ , green, 8–12  $\mu\text{m}$  and red, 12–20  $\mu\text{m}$  (spectrum in Fig. 2). More information on the rotational ladders is given in Sect. 2.2.

derive the CO<sub>2</sub> abundance structure using parametrized abundances.

JWST will allow a big leap forward in our observing capabilities at near- and mid-infrared wavelengths, where the inner planet-forming regions of disks emit most of their lines. The spectrometers on board JWST, NIRSPEC and MIRI (Rieke et al. 2015) with their higher spectral resolving power ( $R \approx 3000$ ) compared to *Spitzer* ( $R = 600$ ) will not only separate many blended lines (Pontoppidan et al. 2010) but also boost line-to-continuum ratios allowing detection of individual  $P$ ,  $Q$  and  $R$ -branch lines thus giving new information on the physics and chemistry of the inner disk. Here we simulate the emission spectra of CO<sub>2</sub> and its <sup>13</sup>CO<sub>2</sub> isotopologue from a protoplanetary disk at JWST resolution. We investigate which subset of these lines is the most useful for abundance determinations at different disk heights and point out the importance of detecting the <sup>13</sup>CO<sub>2</sub> feature. We also investigate which features could signify high CO<sub>2</sub> abundances around the CO<sub>2</sub> iceline due to sublimating planetesimals.

## 2. Modelling CO<sub>2</sub> emission

### 2.1. Vibrational states

The structure of a molecular emission spectrum depends on the vibrational level energies and transitions between these levels that can be mediated by photons. Figure 1 shows the vibrational energy level diagram for CO<sub>2</sub> from the HITRAN database

(Rothman et al. 2013). Lines denote the transitions that are dipole allowed. Colours denote the part of the spectrum where features will show up. This colour coding is repeated in Fig. 2 where a model CO<sub>2</sub> spectrum is presented.

CO<sub>2</sub> is a linear molecule with a  $1^1\Sigma_g^+$  ground state. It has a symmetric,  $v_1$ , and an asymmetric,  $v_3$ , stretching mode (both of the  $\Sigma$  type) and a doubly degenerate bending mode,  $v_2$  ( $\Pi$  type) with an angular momentum,  $l$ . A vibrational state is denoted by these quantum numbers as:  $v_1v_2^lv_3$ . The vibrational constant of the symmetric stretch mode is very close to twice that of the bending mode. Due to this resonance, states with the same value for  $2v_1 + v_2$  and the same angular momentum mix. This mixing leads to multiple vibrational levels that have different energies in a process known as Fermi splitting. The Fermi split levels have the same notation as the unmixed state with the highest symmetric stretch quantum number,  $v_1$  and numbered in order of decreasing energy<sup>1</sup>. This leads to the vibrational state notation of:  $v_1v_2^lv_3(n)$  where  $n$  is the numbering of the levels. This full designation is used in Fig. 1. For the rest of the paper we will drop the  $(n)$  for the levels where there is only one variant.

The number of vibrational states in the HITRAN database is much larger than the set of states used here. Not all of the vibrational states are needed to model CO<sub>2</sub> in a protoplanetary disk because some the higher energy levels can hardly be excited, either collisionally or with radiation, so they should not have an impact on the emitted line radiation. We adopt the same levels as used for AGB stars in González-Alfonso & Cernicharo (1999) and add to this set the 03<sup>3</sup>0 vibrational level.

### 2.2. Rotational ladders

The rotational ladder of the ground state is given in Fig. 1. All states up to  $J = 80$  in each vibrational state are included; this rotational level corresponds to an energy of approximately 3700 K (2550  $\text{cm}^{-1}$ ) above the vibrational state energy. The rotational structure of CO<sub>2</sub> is more complex than that of a linear diatomic like CO. This is due to the fully symmetric wavefunction of CO<sub>2</sub> in the ground electronic state. This means that all states of CO<sub>2</sub> need to be fully symmetric to satisfy Bose-Einstein statistics. As a result, not all rotational quantum numbers  $J$  exist in all of the vibrational states: some vibrational states miss all odd or all even  $J$  levels. There are also additional selections on the Wang parity of the states ( $e, f$ ). For the ground vibrational state this means that only the rotational states with even  $J$  numbers are present and that the parity of these states is  $e$ .

The rotational structure is summarized in Table 1. The states with  $v_2 = v_3 = 0$  all have the same rotational structure as the ground vibrational state. The 01<sup>1</sup>0(1) state has both even and odd  $J$  levels starting at  $J = 1$ . The even  $J$  levels have  $f$  parity, while the odd  $J$  levels have  $e$  parity. In general for levels with  $v_2 \neq 0$  and  $v_3 = 0$ , the rotational ladder starts at  $J = v_2$  with an even parity, with the parity alternating in the rotational ladder with increasing  $J$ . For  $v_3 \neq 0$  and  $v_2 = 0$ , only odd  $J$  levels exist if  $v_3$  is odd, whereas only even  $J$  levels exist if  $v_3$  is even. All levels have an  $e$  parity. For  $v_2 \neq 0$  and  $v_3 \neq 0$ , the rotational ladder is the same as for the  $v_2 \neq 0$  and  $v_3 = 0$  case if  $v_3$  is even, whereas the parities relative to this case are switched if  $v_3$  is odd.

<sup>1</sup> For example: Fermi splitting of the theoretical 02<sup>0</sup> and 10<sup>0</sup> levels leads to two levels denoted as 10<sup>0</sup>(1) and 10<sup>0</sup>(2) where the former has the higher energy.

**Table 1.** Rotational structure of the vibrational levels included in the model.

Vibrational level	Lowest $J$	$J$ levels and parity
00 <sup>0</sup> 0(1)	0	even $J$ , $e$
01 <sup>1</sup> 0(1)	1	even $J$ , $f$ ; odd $J$ , $e$
02 <sup>2</sup> 0(1)	2	even $J$ , $e$ ; odd $J$ , $f$
10 <sup>0</sup> 0(1, 2)	0	even $J$ , $e$
03 <sup>3</sup> 0(1)	3	even $J$ , $f$ ; odd $J$ , $e$
11 <sup>1</sup> 0(1, 2)	1	even $J$ , $f$ ; odd $J$ , $e$
00 <sup>0</sup> 1(1)	1	odd $J$ , $e$
01 <sup>1</sup> 1(1)	1	even $J$ , $e$ ; odd $J$ , $f$

### 2.3. Transitions between states

To properly model the emission of infrared lines from protoplanetary disks non-LTE effects must be taken into account. The population of each level was determined by the balance of the transition rates, both radiative and collisional. The radiative transition rates were set by the Einstein coefficients and the ambient radiation field. Einstein coefficients for CO<sub>2</sub> have been well studied, both in the laboratory and in detailed quantum chemical calculations (see e.g. Rothman et al. 2009; Jacquinet-Husson et al. 2011; Rothman et al. 2013; Tashkun et al. 2015, and references therein). These are collected in several databases for CO<sub>2</sub> energy levels and Einstein coefficients such as the Carbon Dioxide Spectroscopic Database (CDSD) (Tashkun et al. 2015) and as part of large molecular databases such as HITRAN (Rothman et al. 2013) and GEISA (Jacquinet-Husson et al. 2011). Here the <sup>12</sup>CO<sub>2</sub> and <sup>13</sup>CO<sub>2</sub> data from the HITRAN database were used. It should be noted that the differences between the three databases are small for the lines considered here, within a few % in line intensity and less than 1% for the line positions.

The HITRAN database gives the energies of the rovibrational levels above the ground state and the Einstein  $A$  coefficients of transitions between them. Only transitions above a certain intensity at 296 K are included in the databases. The weakest lines included in the line list are 13 orders of magnitude weaker than the strongest lines. With expected temperatures in the inner regions of disks ranging from 100–1000 K, no important lines should be missed due to this intensity cut. In the final, narrowed down set of states all transitions that are dipole allowed have been accounted for.

Collisional rate coefficients between vibrational states are collected from literature sources. The measured rate of the relaxation of the 01<sup>1</sup>0 to the 00<sup>0</sup>0 state by collisions with H<sub>2</sub> from Allen et al. (1980) is used. Vibrational relaxation of the 00<sup>0</sup>1 state due to collisions with H<sub>2</sub> is taken from Nevdakh et al. (2003). For the transitions between the Fermi split levels the rate by Jacobs et al. (1975) for collisions between CO<sub>2</sub> with CO<sub>2</sub> is used with a scaling for the decreased mean molecular mass. Although data used here supersede those in Taylor & Bitterman (1969), that paper does give a sense for the uncertainties of the experiments. The different experiments in Taylor & Bitterman (1969) usually agree within a factor of two, and the numbers used here from Allen et al. (1980) and Nevdakh et al. (2003) fall within the spread for their respective transitions. It is thus expected that the accuracy of the individual collisional rate coefficients is better than a factor of two.

No information is available from the literature for pure rotational transitions induced by collisions of CO<sub>2</sub> with other molecules. We therefore adopt the CO rotational collisional rate

coefficients from the LAMDA database (Schöier et al. 2005; Yang et al. 2010; Neufeld 2012). Due to the lack of dipole moment, the critical density for rotational transitions of CO<sub>2</sub> is expected to be very low ( $n_{\text{crit}} < 10^4$  cm<sup>-3</sup>) and thus the exact collisional rate coefficients are not important for the higher density environments considered here. A method similar to Faure & Josselin (2008), Thi et al. (2013), Bruderer et al. (2015) is used to create the full state-to-state collisional rate coefficient matrix. The method is described in Appendix A.

### 2.4. CO<sub>2</sub> spectra

Figure 2 presents a slab model spectrum of CO<sub>2</sub> computed using the RADEX programme (van der Tak et al. 2007). A density of 10<sup>16</sup> cm<sup>-3</sup> was used to ensure close to LTE populations of all levels. A column density of 10<sup>16</sup> cm<sup>-2</sup> was adopted, close to the observed value derived by Salyk et al. (2011b), with a temperature of 750 K and linewidth of 1 km s<sup>-1</sup>. The transitions are labelled at the approximate location of their  $Q$ -branch. The spectrum shows that, due to the Fermi splitting of the bending and stretching modes, the 15  $\mu$ m feature is very broad stretching from slightly shorter than 12  $\mu$ m to slightly longer than 20  $\mu$ m for the absorption in the Earth atmosphere. For astronomical sources, the lines between 14 and 16  $\mu$ m are more realistic targets.

Two main emission features are seen in the spectrum. The strong feature around 4.3  $\mu$ m is caused by the radiative decay of the 00<sup>0</sup>1 vibrational level to the vibrational ground state. As a  $\Sigma - \Sigma$  transition this feature does not have a  $Q$ -branch, but the  $R$  and  $P$  branches are the brightest features in the spectrum in LTE at 750 K. The second strong feature is at 15  $\mu$ m. This emission is caused by the radiative decay of the 01<sup>1</sup>0 vibrational state into the ground state. It also contains small contribution by the 02<sup>2</sup>0  $\rightarrow$  01<sup>1</sup>0 and 03<sup>3</sup>0  $\rightarrow$  02<sup>2</sup>0 transitions. This feature does have a  $Q$ -branch that has been observed both in absorption (Lahuis et al. 2006) and emission (Carr & Najita 2008; Pontoppidan et al. 2010). The CO<sub>2</sub>  $Q$ -branch is found to be narrow compared to the other  $Q$ -branches of HCN and C<sub>2</sub>H<sub>2</sub> measured in the same sources.

The narrowness is partly due to the fact that the CO<sub>2</sub>  $Q$ -branch is intrinsically narrower than the same feature for HCN. This is connected with the change in the rotational constant between the ground and excited vibrational states. A comparison between  $Q$ -branch profiles for CO<sub>2</sub> and HCN for two optically thin LTE models is presented in Fig. 3. The lighter HCN has a full width half maximum (FWHM) that is about 50% larger than that of CO<sub>2</sub>. The difference in the observed width of the feature is generally larger (Salyk et al. 2011b): the HCN feature is typically twice as wide as the CO<sub>2</sub> feature. Thus the inferred temperature from the CO<sub>2</sub>  $Q$ -branch from the observations is low compared to the temperature inferred from the HCN feature. The difference is amplified by the intrinsically narrower CO<sub>2</sub>  $Q$ -branch, making it more striking.

### 2.5. Dependence on kinetic temperature, density and radiation field

The excitation of, and the line emission from, a molecule depend strongly on the environment of the molecule, especially the kinetic temperature, radiation field and collisional partner density. In Fig. 4 slab model spectra of CO<sub>2</sub> for different physical parameters are compared. The dependence on the radiation field is modelled by including a blackbody field of 750 K diluted with a

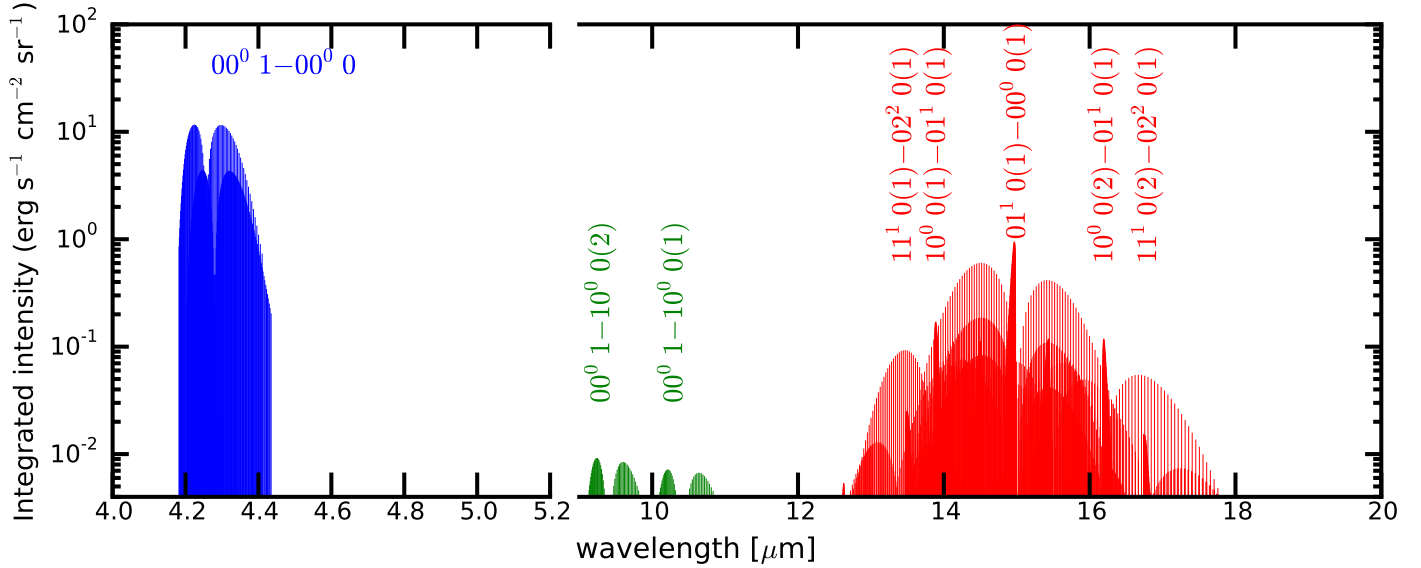


**Fig. 2.** CO<sub>2</sub> slab model spectrum calculated with RADEX (van der Tak et al. 2007), each line in the spectrum is plotted separately. Slab model parameters are: density,  $10^{16}$  cm<sup>-3</sup>; column density of CO<sub>2</sub>,  $10^{16}$  cm<sup>-2</sup>; kinetic temperature, 750 K and linewidth, 1 km s<sup>-1</sup>. For these densities, the level populations are close to local thermal equilibrium (LTE). Spectrum and label colour correspond to the colours in Fig. 1

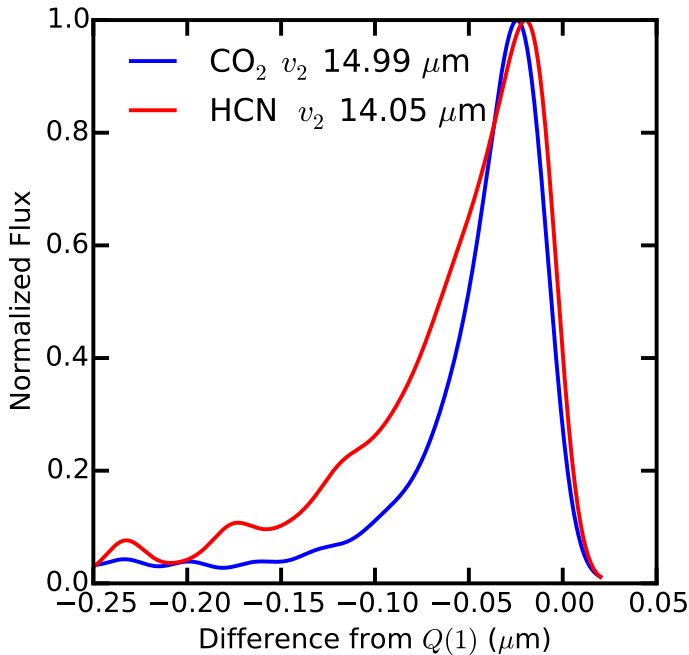


**Fig. 3.**  $v_2$  Q-branch profile of CO<sub>2</sub> and HCN at a temperature of 400 K. Flux is plotted as function of the offset from the lowest energy line (wavelength given in the legend). The lines are convolved to a resolving power  $R = 600$  appropriate for *Spitzer* data. The full width half maximum (FWHM) for CO<sub>2</sub> and HCN are 0.4 and 0.6  $\mu$ m respectively.

factor  $W$ :  $\langle J_v \rangle = WB_v(T_{\text{rad}})$  with  $T_{\text{rad}} = 750$  K. When testing the effects of the kinetic temperature and density, no incident radiation field is included ( $W = 0$ ).

Figure 4 shows that at a constant density of  $10^{12}$  cm<sup>-3</sup> the 4.3  $\mu$ m band is orders of magnitude weaker than the 15  $\mu$ m band. The 15  $\mu$ m band increases in strength and also in width, with increasing temperature as higher  $J$  levels of the CO<sub>2</sub>  $v_2$  vibrational mode can be collisionally excited. Especially the spectrum at 1000 K shows additional Q branches from transitions originating

from the higher energy  $10^0 0(1)$  and  $10^0 0(2)$  vibrational levels at 14 and 16  $\mu$ m.

In the absence of a pumping radiation field, collisions are needed to populate the higher energy levels. With enough collisions, the excitation temperature becomes equal to the kinetic temperature. The density at which the excitation temperature of a level reaches the kinetic temperature depends on the critical density:  $n_c = A_{ul}/K_{ul}$  for a two-level system, where  $A_{ul}$  is the Einstein  $A$  coefficient from level  $u$  to level  $l$  and  $K_{ul}$  is the collisional rate coefficient between these levels. For densities below the critical density the radiative decay is much faster than the collisional excitation and de-excitation. This means that the line intensity scales as  $n/n_c$ . Above the critical density collisional excitation and de-excitation are fast: the intensity is then no longer dependent on the density. The critical density of the 15  $\mu$ m band is close to  $10^{12}$  cm<sup>-3</sup>, so there is little change in this band when increasing the density above this value. However, when decreasing the density below the critical value this results in a strong reduction of the band strength. The critical density of the 4.3  $\mu$ m feature is close to  $10^{15}$  cm<sup>-3</sup> so below this the lines are orders of magnitude weaker than would be expected from LTE.

Adding a radiation field has a significant impact on both the 4.3 and 15  $\mu$ m features. The radiation of a black body of 750 K peaks around 3.8  $\mu$ m so the 4.3  $\mu$ m/15  $\mu$ m flux ratio in these cases is larger than the flux ratio without radiation field for densities below the critical density of the 4.3  $\mu$ m lines. Another difference between the collisionally excited and radiatively excited states is that in the latter case vibrational levels that cannot be directly excited from the ground state by photons, such as the  $10^0 0(1)$  and  $10^0 0(2)$  levels, are barely populated at all.

### 3. CO<sub>2</sub> emission from a protoplanetary disk

To properly probe the chemistry in the inner disk from infrared line emission one needs to go beyond slab models with their inherent degeneracies. A protoplanetary disk model such as that used here includes more realistic geometries and contains a broad range of physical conditions constrained by observational data. Information can be gained on the location and extent of

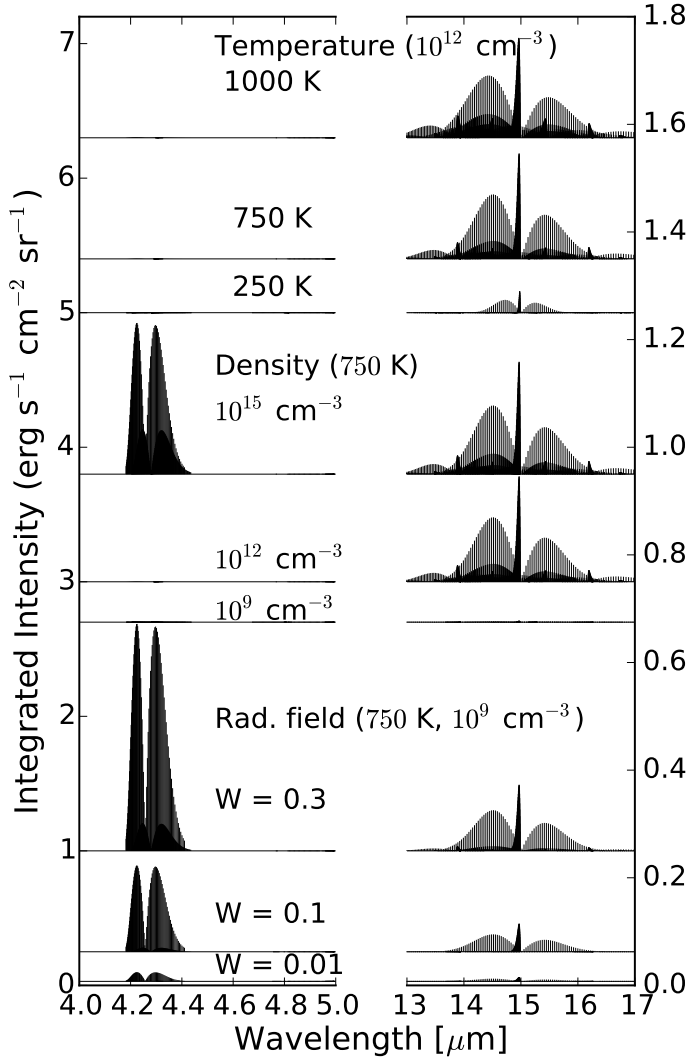


**Fig. 4.** CO<sub>2</sub> slab model spectra for multiple kinetic temperatures, densities and radiation fields. For all the cases the CO<sub>2</sub> column density is kept at 10<sup>16</sup> cm<sup>-2</sup> and the intrinsic linewidth is set to 1 km s<sup>-1</sup>. The spectra are offset for clarity. All spectra are calculated with RADEX (van der Tak et al. 2007).

the emitting CO<sub>2</sub> region as well as the nature of the excitation process. By comparing with observational data, molecular abundances can be inferred as function of location. A critical aspect of the models is the infrared continuum radiation field, which has to be calculated accurately throughout the disk. This means that detailed wavelength dependent dust opacities need to be included and dust temperatures have to be calculated on a very fine grid, since the pumping radiation can originate in a different part of the disk than the lines, for example, the near-infrared for close to the inner rim. The dust is also important in absorbing some of the line flux, effectively hiding parts of the disk from our view.

In this section, the CO<sub>2</sub> spectra are modelled using the DALI (Dust and Lines) code (Bruderer et al. 2012; Bruderer 2013). The focus is on emission from the 15 μm lines that have been observed with *Spitzer* and will be observable with JWST-MIRI. Trends in the shape of the  $\nu_2$  Q-branch and the ratios of lines in the P- and R-branches are investigated and predictions are presented. First the model and its parameters are introduced and the results of one particular model are used as illustration. Finally the effects of various parameters on the resulting line fluxes

are shown, in particular source luminosity and gas/dust ratio. As in Bruderer et al. (2015), the model is based on the source AS 205 (N) but should be representative of a typical T Tauri disk.

### 3.1. Model setup

Details of the full DALI model and benchmark tests are reported in Bruderer et al. (2012) and Bruderer (2013). Here we use the same parts of DALI as in Bruderer et al. (2015). The model starts with the input of a dust and gas surface density structure. The gas and dust structures are parametrized with a surface density profile

$$\Sigma(R) = \Sigma_c \left( \frac{R}{R_c} \right)^{-\gamma} \exp \left[ - \left( \frac{R}{R_c} \right)^{2-\gamma} \right] \quad (1)$$

and vertical distribution

$$\rho(R, \Theta) = \frac{\Sigma(R)}{\sqrt{2\pi}Rh(R)} \exp \left[ - \frac{1}{2} \left( \frac{\pi/2 - \Theta}{h(R)} \right)^2 \right], \quad (2)$$

with the scale height angle  $h(R) = h_c(R/R_c)^\psi$ . The values of the parameters for the AS 205 (N) disk are taken from Andrews et al. (2009) who fitted both the SED and submillimeter images simultaneously. As the inferred structure of the disk is strongly dependent on the dust opacities and size distribution, the same values from Andrews et al. (2009) are used. They are summarized in Table 2 and the gas density structure is shown in Fig. 5, panel a. The central star is a T Tauri star with excess UV due to accretion. All the accretion luminosity is assumed to be released at the stellar surface as a 10<sup>4</sup> K blackbody. The density and temperature profile are typical for a strongly flared disk as used here. The temperature, radiation field and CO<sub>2</sub> excitation structure can be found in the Appendix, Fig. C.1.

In setting up the model special care was taken at the inner rim, where optical and UV photons are absorbed by the dust over a very short physical path. To properly get the temperature structure of the disk directly after the inner rim, high resolution in the radial direction is needed. Varying the radial width of the first cells showed that the temperature structure only converges when the cell width of the first handful of cells is smaller than the mean free path of the UV photons.

The model dust structure is irradiated by the star and the interstellar radiation field. A Monte-Carlo radiative transfer module calculates the dust temperature and the local radiation field at all positions throughout the disk. The gas temperature is then assumed to be equal to the dust temperature. This is not true for the upper and outer parts of the disk. For the regions where CO<sub>2</sub> is abundant in our models the difference between dust temperature and gas temperature computed by self-consistently calculating the chemistry and cooling is less than 5%. The excitation module calculates the CO<sub>2</sub> level populations, using a 1+1D escape probability that includes the continuum radiation due to the dust (Appendix A.2 in Bruderer 2013). Finally the synthetic spectra are derived using the ray tracing module, which solves the radiative transfer equation along rays through the disk. The ray tracing module as presented in Bruderer et al. (2012) is used as well as a newly developed ray-tracing module that is presented in Appendix B which is orders of magnitude faster, but a few percent less accurate. In the ray-tracing module a thermal broadening and turbulent broadening with  $FWHM \sim 0.2$  km s<sup>-1</sup> is used, which means that thermal broadening dominates above  $\sim 40$  K. The gas is in Keplerian rotation around the star. This approach is similar to Meijerink et al. (2009) and Thi et al. (2013)

**Table 2.** Adopted standard model parameters for the AS 205 (N) star plus disk.

Parameter		Value
<b>Star</b>		
Mass	$M_{\star} [M_{\odot}]$	1.0
Luminosity	$L_{\star} [L_{\odot}]$	4.0
Effective temperature	$T_{\text{eff}} [\text{K}]$	4250
Accretion luminosity	$L_{\text{accr}} [L_{\odot}]$	3.3
Accretion temperature	$T_{\text{accr}} [\text{K}]$	10 000
<b>Disk</b>		
Disk Mass ( $g/d = 100$ )	$M_{\text{disk}} [M_{\odot}]$	0.029
Surface density index	$\gamma$	0.9
Characteristic radius	$R_c [\text{AU}]$	46
Inner radius	$R_{\text{in}} [\text{AU}]$	0.19
Scale height index	$\psi$	0.11
Scale height angle	$h_c [\text{rad}]$	0.18
<b>Dust properties<sup>a</sup></b>		
Size	$a [\mu\text{m}]$	0.005–1000
Size distribution		$dn/da \propto a^{-3.5}$
Composition		ISM
Gas-to-dust ratio		100
Distance	$d [\text{pc}]$	125
Inclination	$i [^{\circ}]$	20

**Notes.** <sup>(a)</sup> Dust properties are the same as those used in Andrews et al. (2009) and Bruderer et al. (2015). Dust composition is taken from Draine & Lee (1984) and Weingartner & Draine (2001).

for H<sub>2</sub>O and CO respectively. However Thi et al. (2013) used a chemical network to determine the abundances, whereas here only parametric abundance structures are used to avoid the added complexity and uncertainties of the chemical network.

The adopted CO<sub>2</sub> abundance is either a constant abundance or a jump abundance profile. The abundance throughout the paper is defined as the fractional abundance w.r.t  $n_{\text{H}} = n(\text{H}) + 2n(\text{H}_2)$ . The inner region is defined by  $T > 200$  K and  $A_V > 2$  mag, which is approximately the region where the transformation of OH into H<sub>2</sub>O is faster than the reaction of OH with CO to form CO<sub>2</sub>. The outer region is the region of the disk with  $T < 200$  K or  $A_V < 2$  mag, where the CO<sub>2</sub> abundance is expected to peak. No CO<sub>2</sub> is assumed to be present in regions with  $A_V < 0.5$  mag as photodissociation is expected to be very efficient in this region. The physical extent of these regions is shown in panel b of Fig. 5.

As shown by Meijerink et al. (2009) and Bruderer et al. (2015), the gas-to-dust (“G/D”) ratio is very important for the resulting line fluxes as the dust photosphere can hide a large portion of the potentially emitting CO<sub>2</sub>. Here the gas-to-dust ratio is changed in two ways, by increasing the amount of gas, or by decreasing the amount of dust. When the gas mass is increased and thus the dust mass kept at the standard value of  $2.9 \times 10^{-4} M_{\odot}$ , this is denoted by  $g/d_{\text{gas}}$ . If the dust mass is decreased and the gas mass kept at  $0.029 M_{\odot}$  this is denoted by  $g/d_{\text{dust}}$ .

### 3.2. Model results

Panel c of Fig. 5 presents the contribution function for one of the 15  $\mu\text{m}$  lines, the  $v_2 1 \rightarrow 0 Q(6)$  line. The contribution function shows the relative, azimuthally integrated contribution to the total integrated line flux. Contours show the areas in which 25% and 75% of the emission is located. Panel c also includes

the  $\tau = 1$  surface for the continuum due to the dust, the  $\tau = 1$  surface for the  $v_2 1 \rightarrow 0 Q(6)$  line and surface where the density is equal to the critical density. The area of the disk contributing significantly to the emission is large, an annulus from approximately 0.7 to 30 AU. The dust temperature in the CO<sub>2</sub> emitting region is between 100 and 500 K and the CO<sub>2</sub> excitation temperature ranges from 100–300 K (see Fig. C.1). The density is lower than the critical density at any point in the emitting area.

Panel d of Fig. 5 shows the contribution for the  $v_3 1 \rightarrow 0 R(7)$  line with the same lines and contours as panel c. The critical density for this line is very high,  $\sim 10^{15} \text{ cm}^{-3}$ . This means that except for the inner 1 AU near the mid-plane, the level population of the  $v_3$  level is dominated by the interaction of the molecule with the surrounding radiation field. The emitting area of the  $v_3 1 \rightarrow 0 R(7)$  line is smaller compared to that of the line at 15  $\mu\text{m}$ . The emitting area stretches from close to the sublimation radius up to  $\sim 10$  AU. The excitation temperatures for this line are also higher, ranging from 300–1000 K in the emitting region (see Fig. C.1).

In Fig. 6 the total flux for the  $00^0 1 - 00^0 0 R(7)$  line at 4.25  $\mu\text{m}$  and the 15  $\mu\text{m}$  feature integrated from 14.8 to 15.0  $\mu\text{m}$  are presented as functions of  $x_{\text{out}}$ , for different gas-to-dust ratios and different  $x_{\text{in}}$ . The 15  $\mu\text{m}$  flux shows an increase in flux for increasing total CO<sub>2</sub> abundance and gas-to-dust ratio and so does the line flux of the 4.25  $\mu\text{m}$  line for most of the parameter space. The total flux never scales linearly with abundance, due to different opacity effects. The dust is optically thick at infrared wavelengths up to 100 AU, so there will always be a reservoir of gas that will be hidden by the dust. The lines themselves are strong (have large Einstein  $A$  coefficients) and the natural line width is relatively small (0.2 km s<sup>-1</sup> FWHM). As a result the line centres of transitions with low  $J$  values quickly become optically thick. Therefore, if the abundance, and thus the column, in the upper layers of the disk is high, the line no longer probes the inner regions. This can be seen in Fig. 6 as the fluxes for models with different  $x_{\text{in}}$  converge with increasing  $x_{\text{out}}$ . Convergence happens at lower  $x_{\text{out}}$  for higher gas-to-dust ratios. The inner region is quickly invisible through the 4.25  $\mu\text{m}$  line with increasing gas-to-dust ratios: for a gas-to-dust ratio of 10 000, there is a less than 50% difference in fluxes between the models with different inner abundances, even for the lowest outer abundances. This is not seen so strongly in the 15  $\mu\text{m}$  feature as it also includes high  $J$  lines which are stronger in the hotter inner regions and are not as optically thick as the low  $J$  lines. There is no significant dependence of the flux on the inner abundance of CO<sub>2</sub> if the outer abundance is  $> 3 \times 10^{-7}$  and the gas to dust ratio is higher than 1000. In these models the 15  $\mu\text{m}$  feature traces part of the inner 1 AU but only the upper layers.

Different ways of modelling the gas-to-dust ratio has little effect on the resulting fluxes. Figure 6 shows the fluxes for a constant dust mass and increasing gas mass for increasing the gas-to-dust ratio, whereas Fig. D.1 in Appendix D shows the fluxes for decreasing dust mass for a constant gas mass. The differences in fluxes are very small for models with the same gas/dust ratio times CO<sub>2</sub> abundance, irrespective of the total gas mass: fluxes agree within 10% for most of the models. This reflects the fact that the underlying emitting columns of CO<sub>2</sub> are similar above the dust  $\tau = 1$  surface. Only the temperature of the emitting gas changes: higher temperatures for gas that is emitting higher up in a high gas mass disk and lower temperatures for gas that is emitting deeper into the disk in a low dust mass disk.

The grey band in Figs. 6 and D.1 shows the range of fluxes observed for protoplanetary disks scaled to a common distance of 125 pc (Salyk et al. 2011b). This figure immediately shows that low CO<sub>2</sub> abundances,  $x_{\text{out}} < 3 \times 10^{-7}$ , are needed to be

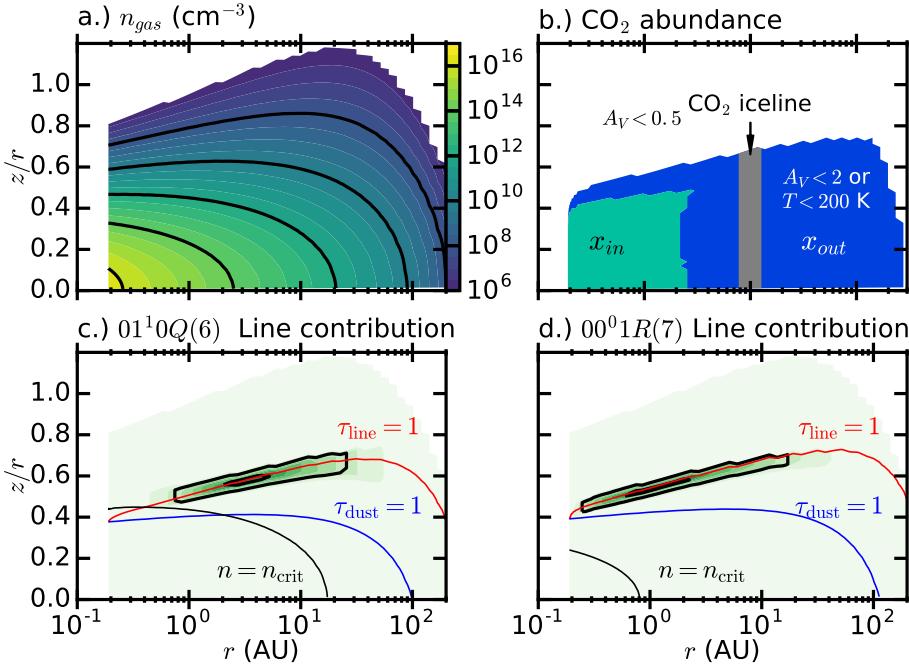


**Fig. 5.** Overview of one of the DALI models showing the disk structure, abundance structure and emitting regions for the  $Q(6) 01^1_0$  and  $R(7) 00^0_1$  lines. The model shown has a gas-to-dust ratio,  $g/d_{\text{gas}} = 1000$  and a constant  $\text{CO}_2$  abundance of  $10^{-7}$  with respect to H. The panels show: **a)** gas density structure; **b)** abundance structure used models:  $x_{\text{in}}$  and  $x_{\text{out}}$  are the  $\text{CO}_2$  abundances in the inner and outer region respectively, the grey region is part of the outer region and denotes the region around the  $\text{CO}_2$  iceline where planetesimals are assumed to vaporize. The abundance in this region is varied in the models in Sect. 4.2; **c)** line contribution function of the  $Q(6) 01^1_0$  line at  $15 \mu\text{m}$ , the contours show the areas in which 25% and 75% of the total flux is emitted; **d)** contribution function for the  $R(7) 00^0_1$  line at  $4.3 \mu\text{m}$ . Panels **c)** and **d)** have the  $\tau = 1$  surface of dust (blue) and line (red) and the  $n = n_{\text{crit}}$  surface (black) overplotted for the relevant line.

consistent with the observations. Some disks have lower fluxes than given by the lowest abundance model, which can be due to other parameters. A more complete comparison between model and observations is made in Sect. 4.1.

In Appendix E a comparison is made between the fluxes of models with  $\text{CO}_2$  in LTE and models for which the excitation of  $\text{CO}_2$  is calculated from the rate coefficients and the Einstein  $A$  coefficients. The line fluxes differ by a factor of about three between the models, similar to the differences found by Bruderer et al. (2015, their Fig. 6) for the case of HCN.

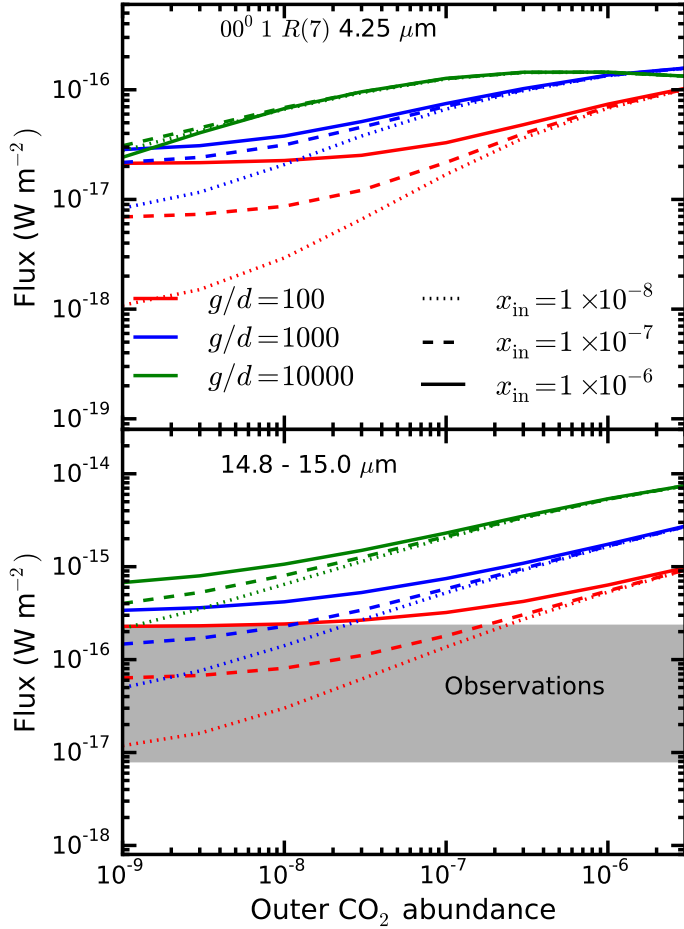
### 3.2.1. The $v_2$ band emission profile

Figure 7 shows the  $v_2$   $Q$ -branch profile at  $15 \mu\text{m}$  for a variety of models. All lines have been convolved to the resolving power of JWST-MIRI at that wavelength ( $R = 2200$ , Rieke et al. 2015; Wells et al. 2015) with three bins per resolution element. Panel a shows the results from a simple LTE slab model at different temperatures whereas panels b and c presents the same feature from the DALI models. Panel b contains models with different gas-to-dust ratios and abundances (assuming  $x_{\text{in}} = x_{\text{out}}$ ) scaled so  $g/d \times x_{\text{CO}_2}$  is constant. It shows that gas-to-dust ratio and abundance are degenerate. It is expected that these models show similar spectra, as the total amount of  $\text{CO}_2$  above the dust photosphere is equal for all models. The lack of any significant difference shows that collisional excitation of the vibrationally excited state is insignificant compared to radiative pumping. Panel c of Fig. 7 shows the effect of different inner abundances on the profile. For the highest inner abundance shown,  $1 \times 10^{-6}$ , an increase in the shorter wavelength flux can be seen, but the differences are far smaller than the differences between the LTE models. Panel d shows models with similar abundances, but with increasing  $g/d_{\text{dust}}$ . The flux in the  $15 \mu\text{m}$  feature increases with  $g/d_{\text{dust}}$  for these models as can be seen in Fig. D.1. This is partly due to the widening of the feature as can be seen in Panel d which is caused by the removal of dust. Due to the lower dust photosphere it is now possible for a larger part of the inner region to contribute to this emission. The inner region is hotter and thus emits more towards high  $J$  lines causing the  $Q$ -branch to widen.

Fitting of LTE models to DALI model spectra in Figs. 7b–d results in inferred temperatures of 300–600 K. Only the models with a strong tail (blue lines in 7b and 7d) need temperatures of 600 K for a good fit, the other models are well represented with  $\sim 300$  K. For comparison, the actual temperature in the emitting layers is 150–350 K (Fig. C.1), illustrating that the optically thin model overestimates the inferred temperatures. The proper inclusion of optical depth effects for the lower- $J$  lines lowers the inferred temperatures. This means that care has to be taken when interpreting a temperature from the  $\text{CO}_2$  profile. A wide feature can be due to high optical depths or high rotational temperature of the gas.

A broader look at the  $\text{CO}_2$  spectrum is thus needed. The left panel of Fig. 8 shows the  $P$ ,  $Q$  and  $R$ -branches of the vibrational bending mode transition at  $R = 2200$ , for models with different inner  $\text{CO}_2$  abundances and the same outer abundance of  $10^{-7}$ . The shape for the  $R$ - and  $P$ -branches is flatter for low to mid- $J$  and slightly more extended at high  $J$  in the spectrum from the model with an inner  $\text{CO}_2$  abundance of  $10^{-6}$  than the other spectra. The peaks at  $14.4 \mu\text{m}$  and  $15.6 \mu\text{m}$  are due to the  $Q$ -branches from the transitions between  $11^1_0(1) \rightarrow 10^0_1(1)$  and  $11^1_0(2) \rightarrow 10^0_1(2)$  respectively. These are overlapping with lines from the bending fundamental  $P$  and  $R$  branches. For the constant and low inner  $\text{CO}_2$  abundances,  $10^{-7}$  and  $10^{-8}$  respectively  $R$ - and  $P$ -branch shapes are similar, with models differing only in absolute flux. Decreasing the inner  $\text{CO}_2$  abundance from  $10^{-8}$  to lower values has no effect of the line strengths.

The right panel of Fig. 8 shows Boltzmann plots of the spectra on the left. The number of molecules in the upper state inferred from the flux is given as a function of the upper state energy. The number of molecules in the upper state is given by:  $N_u = 4\pi d^2 F / (A_{ul} h \nu_{ul} g_u)$ , with  $d$  the distance to the object,  $F$  the integrated line flux,  $g_u$  the statistical weight of the upper level and  $A_{ul}$  and  $\nu_{ul}$  the Einstein  $A$  coefficient and the frequency of the transition. From slope of  $\log(N_u)$  vs.  $E_{\text{up}}$  a rotational temperature can be determined. The expected slopes for 400, 600 and 800 K are given in the figure. It can be seen that the models do not show strong differences below  $J = 20$ , where emission is dominated by optically thick lines. Towards higher  $J$ , the model



**Fig. 6.** Line fluxes as functions of outer CO<sub>2</sub> abundances for models with constant dust mass ( $g/d_{\text{gas}}$ ) and varying gas/dust ratios. The *upper panel* shows the flux of the  $R(7)$  line from the fundamental asymmetric stretch band at  $4.3 \mu\text{m}$ . The *lower panel* shows the flux contained in the  $15 \mu\text{m}$   $Q$ -branch feature. The grey region denotes the full range in CO<sub>2</sub> fluxes from the disks that are reported in Salyk et al. (2011b), scaled to the distance of AS 205 (N). The  $15 \mu\text{m}$  feature contains the flux from multiple  $Q$ -branches with  $\Delta v_2 = 1$ . The CO<sub>2</sub> flux depends primarily on the outer CO<sub>2</sub> abundance and the total  $g/d$  ratio and does not strongly depend on the inner CO<sub>2</sub> abundances. Only for very low outer CO<sub>2</sub> abundances is the effect of the inner abundance on the line fluxes visible. The fluxes for models with  $g/d_{\text{dust}}$  are given in Fig. D.1.

with  $x_{\text{in}} = 10^{-6}$  starts to differ more and more from the other two models. The models with  $x_{\text{in}} = 10^{-7}$  and  $x_{\text{in}} = 10^{-8}$  stay within a factor of two of each other up to  $J = 80$  where the molecule model ends.

Models with similar absolute abundances of CO<sub>2</sub> (constant  $g/d \times x_{\text{CO}_2}$ ) but different  $g/d_{\text{gas}}$  ratios are nearly identical: the width of the  $Q$ -branch and the shapes of the  $P$ - and  $R$ -branches are set by the gas temperature structure. This temperature structure is the same for models with different  $g/d_{\text{gas}}$  ratios as it is set by the dust structure. The temperature is, however, a function of  $g/d_{\text{dust}}$ , but those temperature differences are not large enough for measurable effects. From this it also follows that the exact collisional rate coefficients are not important: the density is low enough that the radiation field can set the excitation of the vibrational levels. At the same time the density is still high enough to be higher than the critical density for the rotational transitions, setting the rotational excitation temperature equal to the gas kinetic temperature.

The branch shapes are a function of  $g/d_{\text{dust}}$  at constant absolute abundance. Apart from the total flux which is slightly higher at higher  $g/d_{\text{dust}}$  (Fig. D.1), the spectra are also broader (Panel d, Fig. 7). This is because the hotter inner regions are less occulted by dust for higher  $g/d_{\text{dust}}$  ratios. This hotter gas has more emission coming from high  $J$  lines, boosting the tail of the  $Q$ -branch.

To quantify the effects of different abundance profiles, line ratios can also be informative. The lines are chosen so they are free from water emission (see Appendix F). The top two panels of Fig. 9 shows the line ratios for lines in the  $01^10(1) \rightarrow 00^00(1)$   $15 \mu\text{m}$  band:  $R(37):R(7)$  and  $P(15):P(51)$ . The  $R(7)$  and  $P(15)$  lines come from levels with energies close to the lowest energy level in the vibrational state (energy difference is less than 140 K). These levels are thus easily populated and the lines coming from these levels are quickly optically thick. The  $R(37)$  and  $P(51)$  lines come from levels with rotational energies at least 750 K above the ground vibrational energy. These lines need high kinetic temperatures to show up strongly and need higher columns of CO<sub>2</sub> at prevailing temperatures to become optically thick. From observation of Fig. 9 a few things become clear. First, for very high outer abundances, it is very difficult to distinguish between different inner abundances based on the presented line ratio. Second, models with high outer abundances are nearly degenerate with models that have a low outer abundance and a high inner abundance. A measure of the optical depth will solve this. In the more intermediate regimes the line ratios presented here or a Boltzmann plot will supplement the information needed to distinguish between a cold, optically thick CO<sub>2</sub> reservoir and a hot, more optically thin CO<sub>2</sub> reservoir that would be degenerate in just  $Q$ -branch fitting.

### 3.2.2. <sup>13</sup>CO<sub>2</sub> $v_2$ band

An easier method to break these degeneracies is to use the <sup>13</sup>CO<sub>2</sub> isotopologue. <sup>13</sup>CO<sub>2</sub> is approximately 68 times less abundant compared to <sup>12</sup>CO<sub>2</sub>, using a standard local interstellar medium value (Wilson & Rood 1994; Milam et al. 2005). This means that the isotopologue is much less likely to be optically thick and thus <sup>13</sup>CO<sub>2</sub>:<sup>12</sup>CO<sub>2</sub> line ratios can be used as a measure of the optical depth, adding the needed information to lift the degeneracies. The bottom panel of Fig. 9 shows the ratio between the flux in the <sup>13</sup>CO<sub>2</sub>  $v_2$   $Q$ -branch and the <sup>12</sup>CO<sub>2</sub>  $v_2$   $P(25)$  line.

As the  $Q$ -branch for <sup>13</sup>CO<sub>2</sub> is less optically thick, it is also more sensitive to the abundance structure. The  $Q$ -branch, situated at  $15.42 \mu\text{m}$ , partially overlaps with the  $P(23)$  line of the more abundant isotopologue so both isotopologues need to be modelled to properly account the contribution of these lines. Figure 10 shows the same models as in Fig. 8 but now with the <sup>13</sup>CO<sub>2</sub> emission in thick lines. The <sup>13</sup>CO<sub>2</sub>  $Q$ -branch is predicted to be approximately as strong as the nearby <sup>12</sup>CO<sub>2</sub> lines for the highest inner abundances. The total flux in the <sup>13</sup>CO<sub>2</sub>  $Q$ -branch shows a stronger dependence on the inner CO<sub>2</sub> abundance than the <sup>12</sup>CO<sub>2</sub>  $Q$ -branch. A hot reservoir of CO<sub>2</sub> strongly shows up as an extended tail of the <sup>13</sup>CO<sub>2</sub>  $Q$ -branch between  $15.38$  and  $15.40 \mu\text{m}$ .

### 3.2.3. Emission from the $v_3$ band

The  $v_3$  band around  $4.25 \mu\text{m}$  is a strong emission band in the disk models, containing a larger total flux than the  $v_2$  band. Even so, the  $4.3 \mu\text{m}$  band of gaseous CO<sub>2</sub> has not been seen in observations of ISO with the Short Wave Spectrometer (SWS) towards high mass protostars in contrast with  $15 \mu\text{m}$  band that has been

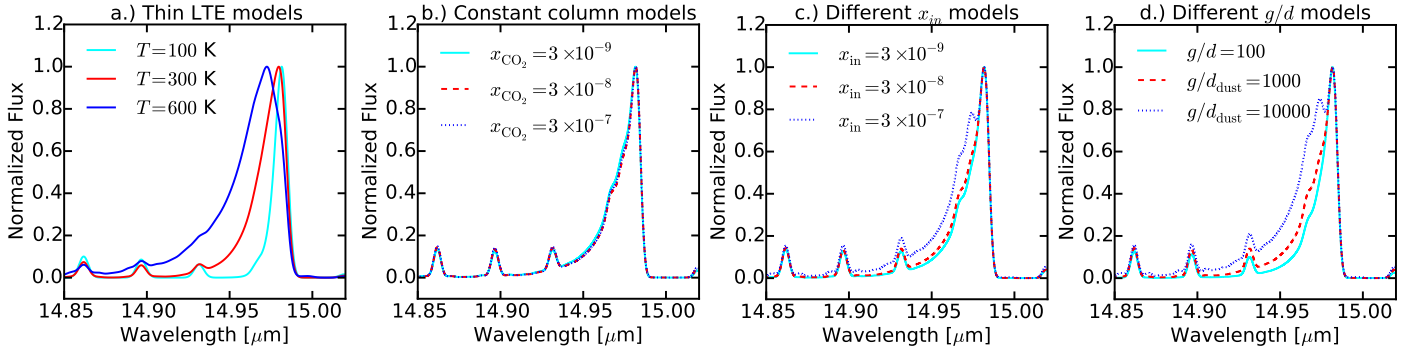


**Fig. 7.**  $Q$ -branch profiles of different models shown at JWST-MIRI resolving power. All fluxes are normalized to the maximum of the feature. In panel **a**) LTE point models with a temperature of 200K (cyan), 400 K (red) and 800 K (blue) are shown. Panel **b**) shows DALI disk models with a constant abundance profile for which the product of abundance times gas-to-dust ratio is constant. All these models have very similar total fluxes. The models shown are  $g/d_{\text{gas}} = 100$ ,  $x_{\text{CO}_2} = 3 \times 10^{-7}$  in red;  $g/d_{\text{gas}} = 1000$ ,  $x_{\text{CO}_2} = 3 \times 10^{-8}$  in blue and  $g/d_{\text{gas}} = 10000$ ,  $x_{\text{CO}_2} = 3 \times 10^{-9}$  in cyan. The spectra are virtually indistinguishable. Panel **c**) shows DALI disk models with a jump abundance profile, a  $g/d_{\text{dust}} = 1000$ , an outer  $\text{CO}_2$  abundance of  $3 \times 10^{-8}$  and an inner abundance of  $3 \times 10^{-7}$  (red),  $3 \times 10^{-8}$  (blue),  $3 \times 10^{-9}$  (cyan). The model with the highest inner abundance shows a profile that is slightly broader than those of the other two. Panel **d**) shows DALI disk models with the same, constant abundance of  $x_{\text{CO}_2} = 3 \times 10^{-8}$ , but with different  $g/d_{\text{dust}}$  ratios. Removing dust from the upper layers of the disk preferentially boosts the high  $J$  lines in the tail of the feature as emission from the dense and hot inner regions of the disk is less occulted by dust.

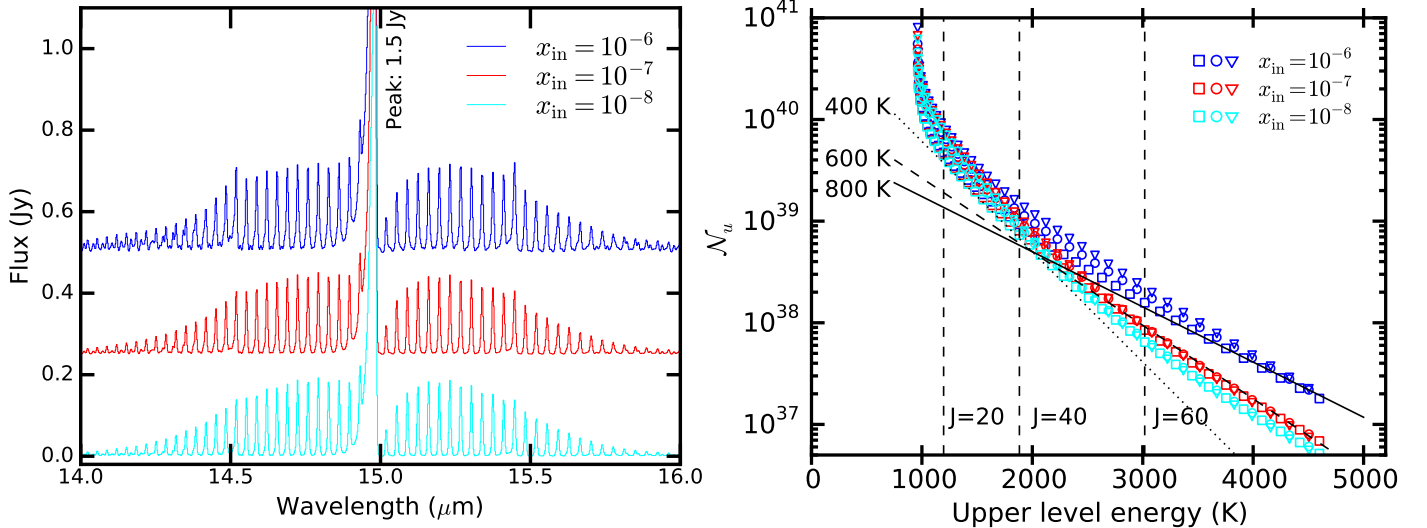


**Fig. 8.** *Left:* full disk spectra at JWST-MIRI resolving power ( $R = 2200$ ) for three disk models with different inner  $\text{CO}_2$  abundances. The outer  $\text{CO}_2$  abundance is  $10^{-7}$  with  $g/d_{\text{gas}} = 1000$ . The models with an inner abundance of  $10^{-8}$  and  $10^{-7}$  are hard to distinguish, with very similar  $P$  and  $R$ -branch shapes. The spectrum of the model with high inner abundances of  $10^{-6}$  are flatter in the region from  $14.6$  to  $14.9 \mu\text{m}$  and the wings are also more extended leading to higher high to mid  $J$  line ratios. *Right:* number of molecules in the upper state as function of the upper level energy inferred from the spectra on the left (Boltzmann plot). Inverse triangles denote the number of molecules inferred from  $P$ -branch lines, squares from  $Q$ -branch lines and circles from  $R$ -branch lines. Vertical dashed lines show the upper level energies of the  $J = 20, 40, 60, v_2 = 1$  levels. The black dotted, dashed and solid lines show the expected slope for a rotational excitation temperature of 400, 600 and 800 K respectively. The near vertical asymptote near upper level energies of 1000 K (the  $v_2 = 1$  rotational ground state energy is due to the regions with large optical depths that dominate the emission from these levels. From around  $J = 20$  the curve flattens somewhat and between  $J = 20$  and  $J = 40$  the curve is well approximated by the theoretical curve for emission from a 400 K gas. At higher  $J$  levels, the model with the highest inner abundance starts to deviate from the other two models as inner and deeper region become more important for the total line emission. Above  $J = 60$  the models in with an inner abundance of  $10^{-8}$  and  $10^{-7}$  are well approximate with a 600 K gas, while the higher inner abundance model is better approximated with a 800 K gas.

seen towards these sources in absorption (van Dishoeck et al. 1996; Boonman et al. 2003a). This may be largely due to the strong solid  $\text{CO}_2$   $4.2 \mu\text{m}$  ice feature obscuring the gas-phase lines for the case of protostars, but for disks this should not be a limitation. Figure 11 shows the spectrum of gaseous  $\text{CO}_2$  in the  $\nu_3$  band around  $4.3 \mu\text{m}$  at JWST-NIRSpec resolving power. The resolving power of NIRSpec is taken to be  $R = 3000$ , which is not enough to fully separate the lines from each other. The  $\text{CO}_2$  emission thus shows up as an extended band.

The band shapes in Fig. 11 are very similar. The largest difference is the strength of the  $4.2 \mu\text{m}$  discontinuity, which is probably an artefact of the model as only a finite number of  $J$  levels are taken into account. The total flux over the whole feature does depend on the inner abundance, but the difference is of the order of  $\sim 10\%$  for 2 orders of magnitude change of the inner abundance.

Figure 11 also shows the  $^{13}\text{CO}_2$  spectrum. The lines from  $^{13}\text{CO}_2$  are mostly blended with much stronger lines from  $^{12}\text{CO}_2$ .

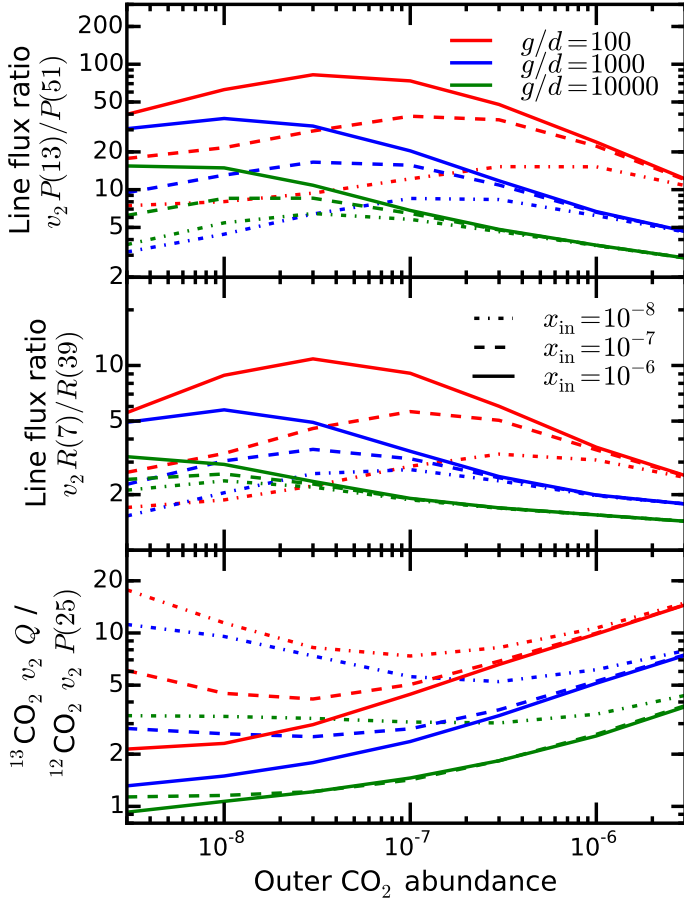


**Fig. 9.** Line ratios as functions of outer abundance, inner abundance and gas to dust ratio ( $g/d_{\text{gas}}$ ). One line ratio in the  $P$  branch ( $P(15):P(51)$ ) (top panel), one line ratio in the  $R$  branch ( $R(7):R(39)$ ) (middle panel) of the  $01^10 \rightarrow 00^00$   $15 \mu\text{m}$  transition are shown together with the line ratio between the  $^{13}\text{CO}_2$   $Q$ -branch and the neighbouring  $^{12}\text{CO}_2$   $P(25)$  line. See the main text for more details.

At the longer wavelength limit,  $^{13}\text{CO}_2$  lines are stronger than those of  $^{12}\text{CO}_2$  but there the  $6 \mu\text{m}$  water band and  $4.7 \mu\text{m}$  CO band start to complicate the detection of  $^{13}\text{CO}_2$  in the  $4\text{--}5 \mu\text{m}$  region.

Average abundances of CO<sub>2</sub> can be derived from observations of the  $4.3 \mu\text{m}$  band. While inferring the abundance structure will be easier from the  $15 \mu\text{m}$  band there are some observational advantages of using the  $4.3 \mu\text{m}$  band. NIRSPEC has multi-object capabilities and will thus be able to get large samples of disks in a single exposure, especially for more distant clusters where there are many sources in a single FOV. NIRSPEC has the additional advantages that it does not suffer from detector fringing and that it is more sensitive (NIRSPEC pocket guide<sup>2</sup>, Rieke et al. 2015; Wells et al. 2015). As both the  $4.3 \mu\text{m}$  and  $15 \mu\text{m}$  bands are pumped by infrared radiation, the flux ratios between these two will mostly contain information about the ratio of the continuum radiation field between the wavelengths of these bands.

### 3.3. Line-to-continuum ratio

The line-to-continuum ratio is potentially an even better diagnostic of the gas/dust ratio than line ratios (Meijerink et al. 2009). In Fig. 12 we present spectra with the continuum added to it. The spectra have been shifted, as the continua for these models

<sup>2</sup> <https://jwst.stsci.edu/>

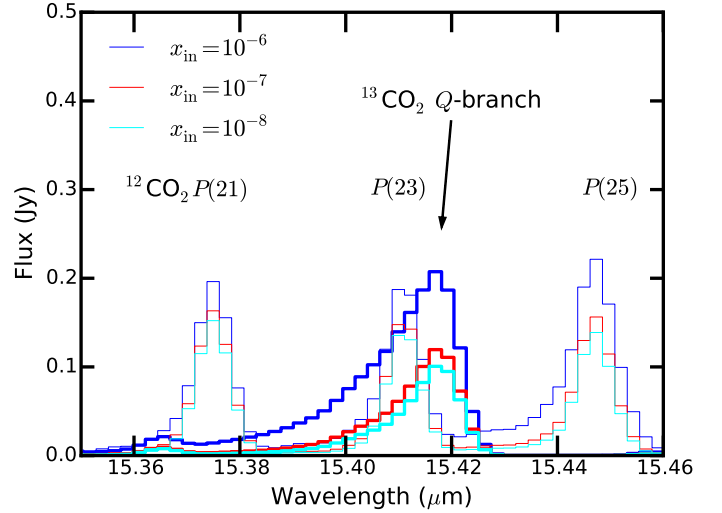


**Fig. 10.** Enlargement of Fig. 8 with  $^{13}\text{CO}_2$  emission added to the spectra (thick lines). The  $^{13}\text{CO}_2$   $Q$ -branch is more sensitive to higher inner abundances.

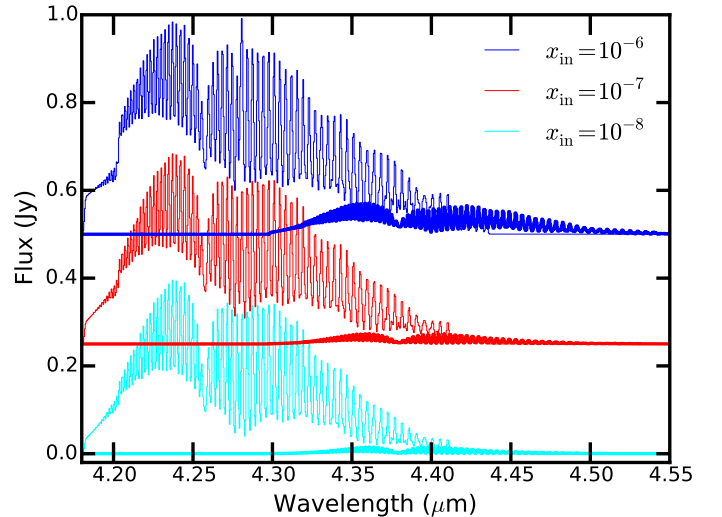


**Fig. 11.** Full disk  $4.3 \mu\text{m}$  spectra at  $R = 3000$  for three disk models with different inner CO<sub>2</sub> abundances. The outer  $^{12}\text{CO}_2$  abundance is  $10^{-7}$  with  $g/d_{\text{gas}} = 1000$ . Thin lines show the emission from  $^{12}\text{CO}_2$ , thick lines the emission from  $^{13}\text{CO}_2$ . For both isotopes individual line peaks can be seen but the lines blend together in the wings forming a single band. Spectra are shifted vertically for display purposes.

overlap. The models for which the spectra are derived all have a CO<sub>2</sub> abundance of  $10^{-8}$  but differ in the gas-to-dust ratio. The gas-to-dust ratio, determines the column of CO<sub>2</sub> that can contribute to the line. A large part of the CO<sub>2</sub> reservoir near the mid-plane cannot contribute due to the large continuum optical depth of the dust. It is thus not surprising that the line-to-continuum ratio is strongly dependent on the gas-to-dust ratio. The precise method for setting the gas-to-dust ratio (by increasing the amount of gas, or decreasing the amount of dust) does not really matter for the line-to-continuum ratio. It does matter for the absolute scaling of the continuum, which decreases if the amount of dust is decreased.

Meijerink et al. (2009) could constrain the gas-to-dust ratio from the data since there is an upper limit to the H<sub>2</sub>O abundance from the atomic O abundance. Here it is not possible to make a similar statement as CO<sub>2</sub> is not expected to be a major reservoir of either the oxygen or the carbon in the disk. On the contrary,

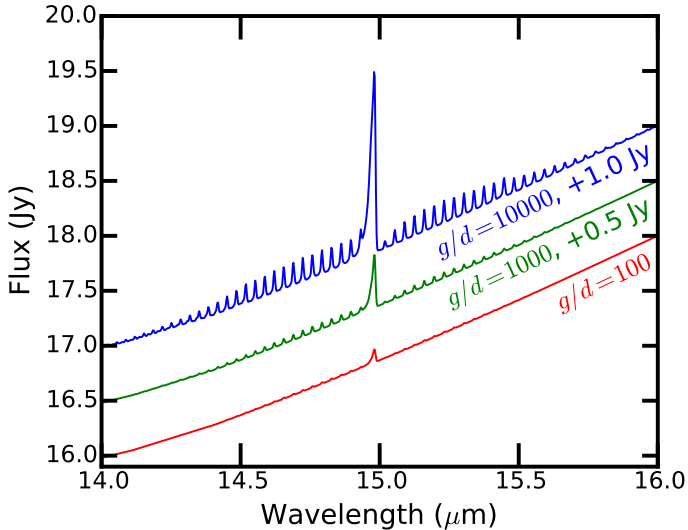


**Fig. 12.** Full disk spectra with added continuum for models with different gas-to-dust ratios. All spectra have been convolved to a spectral resolving power of  $R = 2200$ . All models have the same  $\text{CO}_2$  abundance of  $10^{-8}$ . The spectra have been shifted by the amount shown.

from Fig. 6 it can be seen that with a gas-to-dust ratio of 100 an abundance of  $10^{-7}$  is high enough to explain the brightest of the observed line fluxes. The line-to-continuum ratios from the *Spitzer*-IRS spectra of 5–10% are also matched by the same models (see Fig. 13). External information such as can be obtained from  $\text{H}_2\text{O}$  is needed to lift the degeneracy between high gas-to-dust ratio and high abundance: if one of the two is fixed, the other can be determined from the flux or line-to-continuum ratio.

The line-to-continuum ratio is very important for planning observations, however, as it sets the limit on how precisely the continuum needs to be measured to be able to make a robust line detection. Figure 13 shows the line-to-continuum ratios for models with a constant abundance. These figures show that high signal-to-noise ( $S/N$ ) on the continuum is needed to be able to get robust line detections. The  $^{12}\text{CO}_2$   $Q$ -branch should be easily accessible for most protoplanetary disks. To be able to probe individual  $P$ - and  $R$ -branch lines of the  $^{12}\text{CO}_2$   $15\ \mu\text{m}$  feature as well as the  $^{13}\text{CO}_2$   $Q$ -branch, deeper observations (reaching  $S/N$  of at least 300, up to 1000) will be needed to probe down to disks with  $\text{CO}_2$  abundances of  $10^{-8}$  and gas-to-dust ratios of 1000.

### 3.4. $\text{CO}_2$ from the ground

As noted earlier, there is a large part of the  $\text{CO}_2$  spectrum that cannot be seen from the ground because of atmospheric  $\text{CO}_2$ . There are a few lines, however, that could be targeted from the ground using high spectral resolution. The high  $J$  lines ( $J > 70$ ) of the  $v_1 = 1-0$  transition in the  $R$  branch around  $4.18\ \mu\text{m}$  are visible with a resolving power of  $R = 30\,000$  or higher. At this resolution the  $\text{CO}_2$  atmospheric lines are resolved and at  $J > 70$  they are narrow enough to leave 20–50% transmission windows between them (ESO skycalc<sup>3</sup>). The lines are expected to have a peak line-to-continuum ratio of 1:100. So a  $S/N$  of 10 on the line peak translates to a  $S/N$  of 1000 on the continuum. The FWHM of the atmospheric lines is about  $30\ \text{km s}^{-1}$ . So half of the emission line profile should be observable when the relative velocity

<sup>3</sup> <http://www.eso.org/observing/etc/bin/gen/form?INS.MODE=swspectr+INS.NAME=SKYCALC>

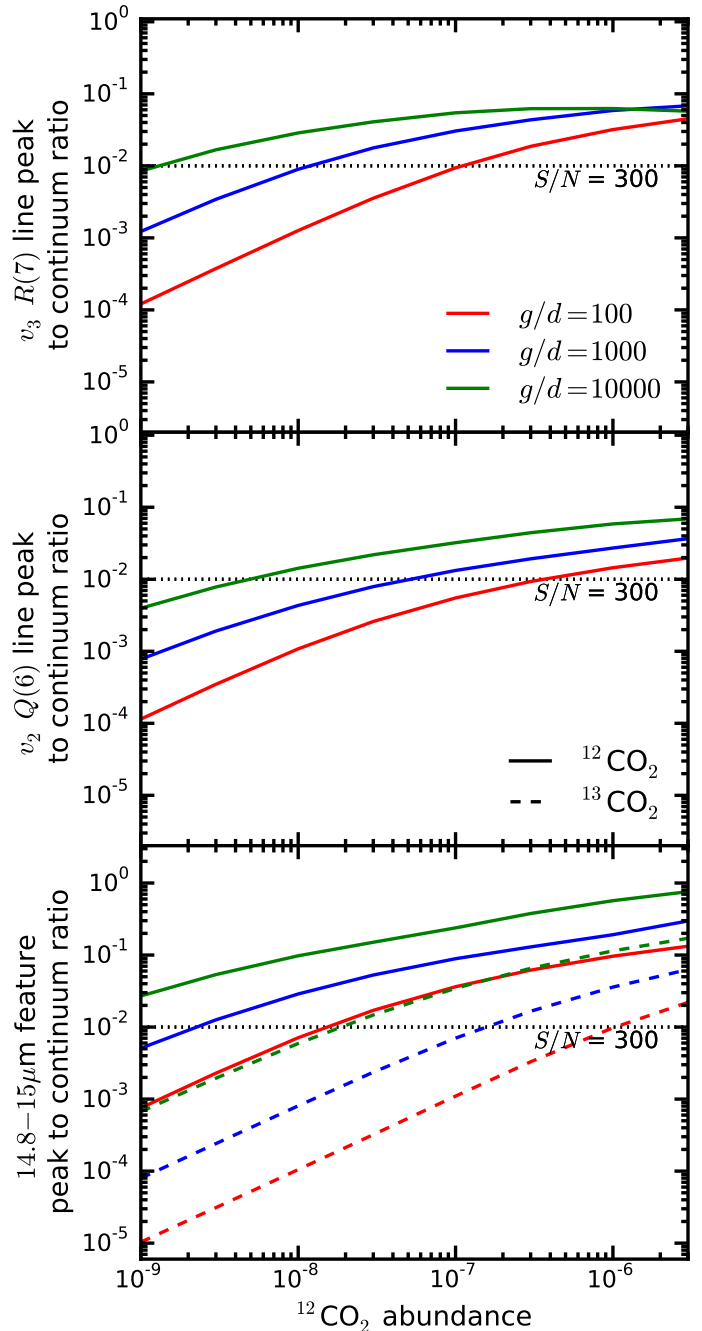


**Fig. 13.** Line-to-continuum for  $^{12}\text{CO}_2$  as function of abundance for different gas-to-dust ratios in solid lines. In the bottom plot the line-to-continuum for  $^{13}\text{CO}_2$   $Q$ -branch is shown in dashed lines. A dotted black line shows a line-to-continuum of 0.01, lines with this line-to-continuum ratio can be observed if the signal-to-noise ( $S/N$ ) on the continuum is more than 300. With a  $S/N$  on the continuum of 300, observations of the  $Q$ -branch should be able to probe down to  $10^{-9}$  in abundance for a gas-to-dust ratio of 1000. With similar gas-to-dust ratio and  $S/N$ , individual lines the  $15\ \mu\text{m}$  band will only be observable in disk with  $\text{CO}_2$  abundances higher than  $3 \times 10^{-8}$ .

shift between observer and source is more than  $15\ \text{km s}^{-1}$ . Since the Earth's orbit allows for velocity shifts up to  $30\ \text{km s}^{-1}$  in both directions, observing the full line profile is possible in two observations at different times of year for sources close to the orbital plane of the earth. The exposure time needed to get a  $S/N$  of 1000 on the continuum at  $4.18\ \mu\text{m}$ , which is  $6.7\ \text{Jy}$  in our AS 205 (N) model, with a 40% sky transmission on the lines, is

about ten hours for VLT-CRIRES<sup>4</sup>. The high  $J$   $P$ -branch lines of CO<sub>2</sub> are close to atmospheric lines from N<sub>2</sub>O, O<sub>3</sub> and H<sub>2</sub>O resulting in a very opaque atmosphere at these wavelengths (Noll et al. 2012; Jones et al. 2013).

The other lines that can be seen from the ground are between 9 and 12  $\mu\text{m}$  (in the  $N$  band). These originate from the  $01^11$  and  $00^01$  levels. The line to continuum ratios vary from 1:40 to 1:3000 for the brighter lines in the  $00^01 \rightarrow 10^00(1)$  band with the most likely models having line to continuum ratios between 1:200 and 1:2000. For a continuum of  $\sim 11$  Jy a  $S/N$  of 2000 for  $R = 10^5$  could potentially be achieved in about three to ten minutes of integration with the European Extremely Large Telescope (E-ELT). At the location of the CO<sub>2</sub> atmospheric absorption lines in this part of the spectrum the sky transmittance is 50% and the atmospheric lines have a FWHM of  $\sim 50$  km s<sup>-1</sup>

### 3.5. CO<sub>2</sub> model uncertainties

The fluxes derived from the DALI models depend on the details of the CO<sub>2</sub> excitation processes included in the model. The collisional rate coefficients are particularly uncertain, since the measured set is incomplete. There are multiple ways to extrapolate what is measured to what is needed to complete the model. Modelling slabs of CO<sub>2</sub> using different extrapolations such as: absolute scaling of the rotational collision rate coefficients, including temperature dependence of the vibrational collisional rate coefficients and different implementations of the collision rate coefficients between the vibrational levels with  $2v_1 + v_2 = \text{constant}$ , show that fluxes can change by up to 50% for specific combinations of radiation fields and densities. The highest differences are seen in the 4–5  $\mu\text{m}$  band, usually at low densities. The flux in the 15  $\mu\text{m}$  band usually stays within 10% of the flux of the model used here. These uncertainties are small compared to other uncertainties in disk modelling such as the chemistry or parameters of the disk hosting protostar. The main reason that the fluxes are relatively insensitive to the details of the collisional rate coefficients is due to the importance of radiative pumping in parallel with collisions.

The assumption  $T_{\text{dust}} = T_{\text{gas}}$  is not entirely correct, since the gas temperature can be up to 5% higher than the dust temperature in the CO<sub>2</sub> emitting regions. This affects our line fluxes. For the 4.3  $\mu\text{m}$  fluxes the induced difference in flux is always smaller than 10%. For the 15  $\mu\text{m}$  fluxes difference are generally smaller than 10%, whereas some of the higher  $J$  lines are up to 25% brighter.

A very simplified abundance structure was taken. It is likely that protoplanetary disks will not have the abundance structure adopted here. Full chemical models indeed show much more complex chemical structures (see e.g. Walsh et al. 2015). The analysis carried out in this work here should still be appropriate for more complex abundance structures, and future work will couple such chemistry models directly with the excitation and radiative transfer.

The stellar parameters for the central star and the exact parameters of the protoplanetary disk also influence the resulting CO<sub>2</sub> spectrum. The central star influences the line emission through its UV radiation that can both dissociate molecules and heat the gas. Since for our models no chemistry is included, only the heating of the dust by stellar radiation is important for our models. The CO<sub>2</sub> flux in the emission band around 15  $\mu\text{m}$  scales

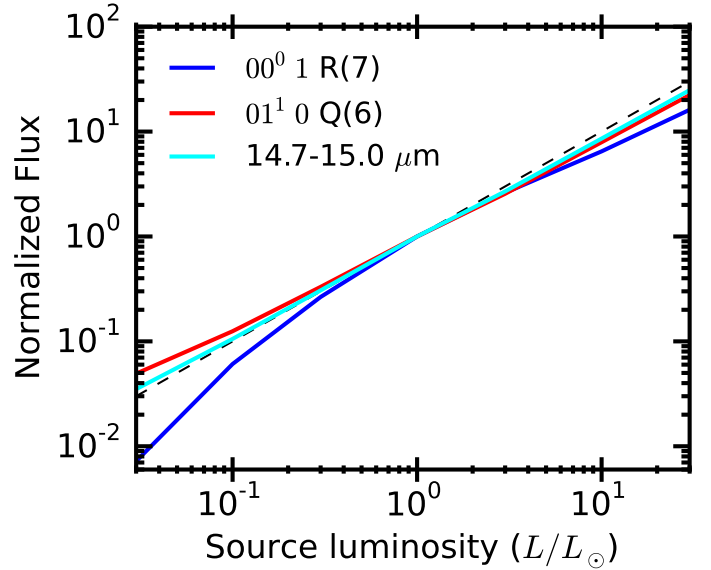


**Fig. 14.** CO<sub>2</sub> flux versus stellar luminosity for three different features in the spectrum. All fluxes have been normalized to the flux of the 1  $L_{\odot}$  model. Both the flux in the 14.7 to 15  $\mu\text{m}$  region, which corresponds to the  $v_2$   $Q$ -branch, and the flux from the  $01^10$   $Q(6)$  line have a nearly linear dependence on the stellar luminosity. The dependence of the  $00^01$   $R(7)$  line at 4.3  $\mu\text{m}$  on source luminosity is more complex.

almost linearly with the bolometric luminosity of the central object (see Fig. 14).

## 4. Discussion

### 4.1. Observed 15 $\mu\text{m}$ profiles and inferred abundances

The  $v_2$  15  $\mu\text{m}$  feature of CO<sub>2</sub> has been observed in many sources with *Spitzer*-IRS (Pontoppidan et al. 2010; Salyk et al. 2011b). The SH (Short-High) mode barely resolves the 15  $\mu\text{m}$   $Q$ -branch, but that is enough to compare with the models. We used the spectra that have been reduced with the Caltech High-res IRS pipeline (CHIP; Pontoppidan et al. 2010; Pontoppidan 2016). The sources selected out of the repository have a strong emission feature of CO<sub>2</sub> but no distinguishable H<sub>2</sub>O emission in the 10–20  $\mu\text{m}$  range. The sources and some stellar parameters are listed in Table 3. The observed spectra are continuum subtracted (Appendix G) and the observed profiles are compared with model profiles by eye (Fig. 15).

Two sets of comparisons are made. For the first set, the model fluxes are only corrected for the distance to the objects. For the other set, the model fluxes are scaled for the distance but also scaled for the luminosity of the central source, using  $L_{\text{CO}_2} \propto L_{\star}$ . This relation is found by running a set of models with a range of luminosities, presented in Fig. 14. Aside from the luminosity of the star, all other parameters have been kept the same including the shape of the stellar spectrum. The effective temperature of the star mostly affects the fraction of short wavelength UV photons which can photodissociate molecules, but since no detailed chemistry is included, the use of a different stellar temperature would not change our results. Other tests (not shown here) have indeed shown that the shape of the spectrum does not really matter for the CO<sub>2</sub> line fluxes in this parametric model. All models have a gas-to-dust ratio of 1000 and a constant CO<sub>2</sub> abundance of  $10^{-8}$ .

Both the total flux in the range between 14.7 and 15.0  $\mu\text{m}$  and that of a single line in this region (the  $01^10$   $Q(6)$  line) have

<sup>4</sup> Exposure times have been calculated with the ESO exposure time calculator <https://www.eso.org/observing/etc/> for CRIRES (version 5.0.1).

an almost linear relation with luminosity of the central star. For the 00<sup>0</sup>1 *R*(7) line around 4.3  $\mu\text{m}$  the dependence on the central luminosity is slightly more complex. Below a stellar luminosity of  $1 L_{\odot}$  the dependence is stronger than linear, but above that the dependence becomes weaker than linear. Overall, it is reasonable to correct the 15  $\mu\text{m}$  fluxes from our model for source stellar luminosities using the linear relationship. This is because the amount of infrared continuum radiation that the disk produces scales linearly with the amount of energy that is put into the disk by the stellar radiation. It is the infrared continuum radiation that sets the molecular emission due to radiative pumping, the dominant vibrational excitation mechanism for CO<sub>2</sub>.

The model spectra are overplotted on the continuum subtracted observations in Fig. 15. The flux in these models has been scaled with the distance of the source and the luminosity of the central star. A gas-to-dust ratio of 1000 is adopted as inferred from H<sub>2</sub>O observations (Meijerink et al. 2009).

An overview of the inferred abundances is given in Table 4. For the DALI models the emitting CO<sub>2</sub> column and the number of emitting CO<sub>2</sub> molecules have been tabulated in Table 4. The column is defined as the column of CO<sub>2</sub> above the  $\tau_{\text{dust}} = 1$  line at the radial location of the peak of the contribution function (Fig. 5d). The number of molecules is taken over the region that is responsible for half the total emission as given by the contribution function. The number of molecules shown is thus the minimum amount of CO<sub>2</sub> needed to explain the majority of the flux and a sets lower limit for the amount of CO<sub>2</sub> needed to explain all of the emission. The inferred abundances range from  $10^{-9}$ – $10^{-7}$ . They agree with that inferred by Pontoppidan & Blewins (2014) using an LTE disk model appropriate for the RNO 90 disk, demonstrating that non-LTE excitation effects are minor (see also Appendix E).

For GW Lup and SZ 50 the emitting CO<sub>2</sub> columns found by Salyk et al. (2011b) are within a factor of two from those inferred here, whereas for DN Tau and IM Lup our inferred columns are consistent with the upper limits from the slab models (tabulated in Table 4). However, the inferred column for HD 101412 differs greatly. For all disks the number of molecules in our models is at least an order of magnitude higher than the number of molecules inferred from the LTE models. The emitting area used by Salyk et al. (2011b) in fitting the CO<sub>2</sub> feature was fixed and generally taken to be slightly larger than the inner 1 AU. This is very small compared to the emitting area found in this work which extends up to 30 AU. It is thus unsurprising that the total number of CO<sub>2</sub> molecules inferred is lower for the LTE slab models from Salyk et al. (2011b). The high number of molecules needed for the emission in our models is also related to the difference in excitation: the vibrational excitation temperature of the gas in the non-LTE models is lower (100–300 K) than the temperature fitted for the LTE models (~650 K). Thus in the non-LTE models a larger number of molecules is needed to get the same total flux. The narrow CO<sub>2</sub> profile is due to low rotational temperatures as emission from large radii >2–10 AU dominates the strongest lines. The visual contrast is enhanced by the fact that the CO<sub>2</sub> feature is also intrinsically narrower at similar temperatures than that of HCN (Fig. 3). For HD 101412 the model feature is notably narrower than the observed feature signifying either a higher CO<sub>2</sub> rotational temperature, or a more optically thick emitting region.

There are of course caveats in the comparisons done here. The standard model uses a T Tauri star that is luminous (total luminosity of  $7.3 L_{\odot}$ ) and that disk is known to have very strong H<sub>2</sub>O emission. The sample of comparison protostars consists of 7 T Tauri stars that have luminosities a factor of 2–35 lower than

assumed in our model and a Herbig Ae star that is more than three times as luminous. A simple correction for source luminosity is only an approximation. All of these sources have little to no emission lines of H<sub>2</sub>O in the mid-infrared. This may be an indication of different disk structures, and the disk model used in this work may not be representative of these water-rich disks. Indeed, Banzatti & Pontoppidan (2015) found that the emitting radius of the CO ro-vibrational lines scales inversely with the vibrational temperature inferred from the CO emission. This relation is consistent with inside-out gap opening. Comparing the CO ro-vibrational data with H<sub>2</sub>O infrared emission data from VLT-CRIRES and *Spitzer*-IRS Banzatti et al. (2017) found that there is a correlation between the radius of the CO ro-vibrational emission and the strength of the water emission lines: the larger the radius of the CO emission, the weaker the H<sub>2</sub>O emission. This suggests that the H<sub>2</sub>O-poor sources may also have inner gaps, where both CO and H<sub>2</sub>O are depleted. There are only two H<sub>2</sub>O-poor sources in our sample that overlap with Banzatti et al. (2017).

However, if our analysis is applied to sources that do have water emission, the range of best-fit CO<sub>2</sub> abundances is found to be similar. Figure G.2 shows CO<sub>2</sub> model spectra compared to observations for a set of the strongest water emitting sources. The conclusion that the abundance of CO<sub>2</sub> in protoplanetary disks is around  $10^{-8}$  is, therefore, robust.

The inferred CO<sub>2</sub> abundances are low, much lower than the expected ISM value of  $10^{-5}$  if all of the CO<sub>2</sub> would result from sublimated ices. This demonstrates that the abundances have been reset by high temperature chemistry, as also concluded by Pontoppidan & Blewins (2014).

The inferred low abundances agree well with chemical models by Walsh et al. (2015). However, the column found for chemical models by Agúndez et al. (2008),  $\sim 6 \times 10^{16} \text{ cm}^{-2}$ , is more than an order of magnitude higher. Agúndez et al. (2008) used a different lower vertical bound for their column integration and only considered the inner 3 AU. Either of these assumptions may explain the difference in the CO<sub>2</sub> column.

#### 4.2. Tracing the CO<sub>2</sub> iceline

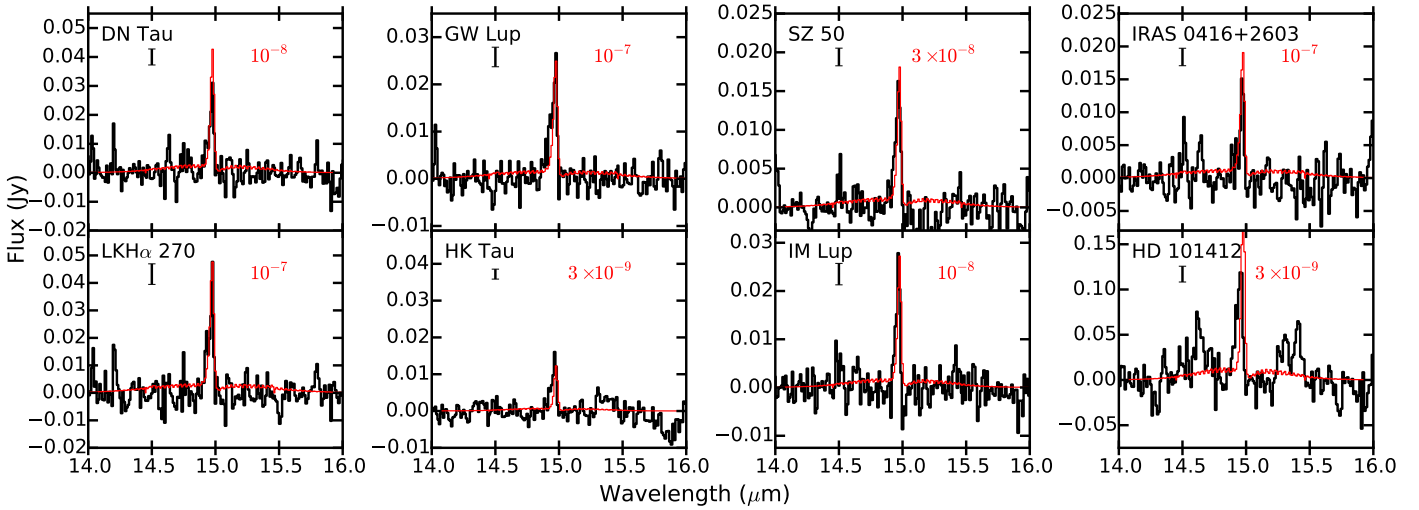
One of the new big paradigms in (giant) planet formation is pebble accretion. Pebbles, in models defined as dust particles with a Stokes number around one, are badly coupled to the gas, but generally not massive enough to ignore the interaction with the gas. This means that these particles settle to the mid-plane and radially drift inward on short time scales. This pebble flux allows in theory a planetesimal to accrete all the pebbles that form at radii larger than its current location (Ormel & Klahr 2010; Lambrechts & Johansen 2012; Levison et al. 2015).

This flux of pebbles also has consequences for the chemical composition of the disk. These pebbles should at some point encounter an iceline, if they are not stopped before. At the iceline they should release the corresponding volatiles. The same holds for any drifting planetesimals (Ciesla & Cuzzi 2006). As the ice composition is very different from the gas composition, this can in principle strongly change the gas content in a narrow region around the ice line. For this effect to become observable in mid-infrared lines, the sublimated ices should also be mixed vertically to higher regions in the disk.

From chemical models the total gas-phase abundance of CO<sub>2</sub> around the CO<sub>2</sub> iceline is thought to be relatively low, ( $10^{-8}$ , Walsh et al. 2015) similar to the value found in this work. The CO<sub>2</sub> ice content in the outer disk can be orders of magnitude higher. Both chemical models and measurements of comets

**Table 3.** Stellar parameters.

Object	Source luminosity ( $L_{\odot}$ )	Spectral type	Stellar mass ( $M_{\odot}$ )	Distance (pc)	References
DN Tau/Sz 82	1.62	M0	0.62	140	Rigliaco et al. (2015)
GW Lup/Sz 71	0.3	M1.5	0.42	150	Alcalá et al. (2014)
SZ50	0.57	M4	0.27	178	Manara et al. (2016)
IRAS 04216+2603	0.2	M0	0.57	140	Rigliaco et al. (2015), Andrews et al. (2013)
LkH $\alpha$ 270	1.4	K2	?	235	Winston et al. (2010)
HK Tau	1.12	M0.5	0.56	140	Rigliaco et al. (2015)
IM Lup	3.53	M0	0.56	190	Rigliaco et al. (2015)
HD 101412	25	A0	2.3	160	van der Plas et al. (2008)


**Fig. 15.** Continuum subtracted spectra (black) with DALI CO<sub>2</sub> emission models (red) for the eight selected sources. The abundance used in the DALI model is given in each frame, taken to be constant over the whole disk. The line fluxes have been corrected for the distances to the sources. The errorbar in the top left corner of each panel shows the median errorbar on the data.

**Table 4.** Inferred CO<sub>2</sub> abundances from *Spitzer* data.

Object	Inferred abundance (w.r.t H)		Salyk et al. (2011b) LTE slab results		DALI Non-LTE results	
	$d$ corr.	$d$ and $L_{\star}$ corr.	Column ( $\text{cm}^{-2}$ )	$N_{\text{tot,CO}_2}$ (mol.)	Column ( $\text{cm}^{-2}$ )	$N_{\text{tot,CO}_2}$ (mol.) <sup>a</sup>
DN Tau	1(-9)	1(-8)	<5.0(14)	<3.8(41)	2(14)	2(44)
GW Lup	1(-9)	1(-7)	1.5(15)	1.1(42)	2(15)	8(44)
SZ50	1(-9)	3(-8)	1.0(15)	7.6(41)	7(14)	5(44)
IRAS 04216+2603	<1(-9)	1(-7)	–	–	2(15)	8(44)
LkH $\alpha$ 270	0.3-1(-8)	1(-7)	3.9(15)	4.1(42)	2(15)	8(44)
HK Tau	<1(-9)	3(-9)	–	–	5(13)	1(44)
IM Lup	1-3(-9)	1(-8)	<7.9(14)	<6.9(41)	2(14)	2(44)
HD 101412	1(-8)	1-3(-9)	1.0(16)	1.94(43)	2-5(13)	0.7-1(44)

**Notes.**  $a(b) = a \times 10^b$ . <sup>(a)</sup> Minimal number of CO<sub>2</sub> molecules responsible for half of the emission.

show that the CO<sub>2</sub> content in ices can be more than 20% of the total ice content (Le Roy et al. 2015; Eistrup et al. 2016), with CO<sub>2</sub> ice even becoming more abundant than H<sub>2</sub>O ice in some models of outer disk chemistry (Drozdovskaya et al. 2016). This translates into an abundance up to a few  $\times 10^{-5}$ . Here, we investigate whether the evaporation of these CO<sub>2</sub> ices around the iceline would be observable.

To model the effect of pebbles moving over the iceline, a model with a constant CO<sub>2</sub> abundance of  $1 \times 10^{-8}$  and a gas-to-dust ratio of 1000 is taken. In addition, the abundance of CO<sub>2</sub> is enhanced in an annulus where the midplane temperature is between 70 K and 100 K (grey region in Fig. 5b), corresponding

to the sublimation temperature of pure CO<sub>2</sub> ice (Harsono et al. 2015). This results in a radial area between 8 and 15 AU in our case. The abundance is taken to be enhanced over the total vertical extent of the CO<sub>2</sub> in the model, as in the case of strong vertical mixing. The spectra from three models with enhanced abundances of  $x_{\text{CO}_2, \text{ring}} = 10^{-6}$ ,  $10^{-5}$  and  $10^{-4}$  in this ring can be seen in Fig. 16 together with the spectrum for the constant  $x_{\text{CO}_2} = 10^{-8}$  model. We note that CO<sub>2</sub> ice is unlikely to be pure, and that some of it will likely also come off at the H<sub>2</sub>O iceline, but such a multi-step sublimation model is not considered here.

The spectra in Fig. 16 show both <sup>12</sup>CO<sub>2</sub> and <sup>13</sup>CO<sub>2</sub> for the model with a constant abundance, an enhanced abundance of

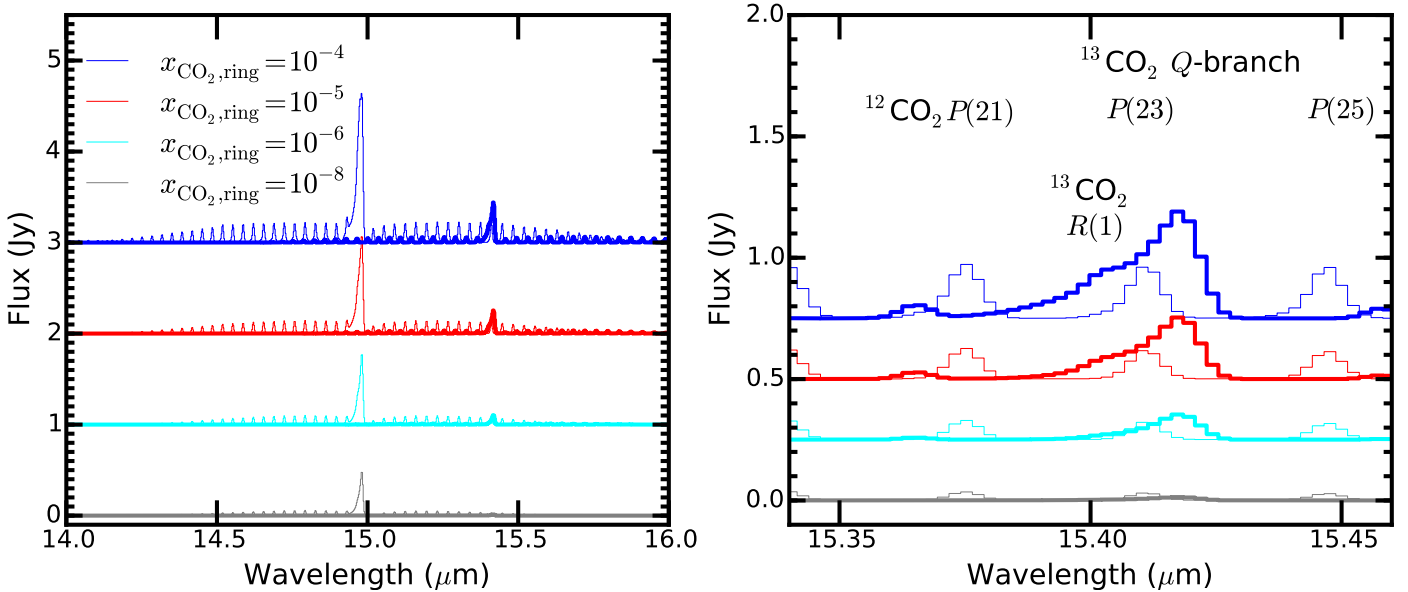


**Fig. 16.**  $^{12}\text{CO}_2$  (thin lines) and  $^{13}\text{CO}_2$  spectra (thick lines) of models with an enhanced  $\text{CO}_2$  abundance around the  $\text{CO}_2$  iceline. The models have a constant abundance of  $\text{CO}_2$  of  $10^{-8}$  throughout most of the disk. The grey lines denote the model without any local enhancements in the  $\text{CO}_2$  abundance in an annulus around the  $\text{CO}_2$  iceline. The cyan, red and blue lines show the models with an enhanced abundance of  $10^{-6}$ ,  $10^{-5}$  and  $10^{-4}$ , respectively. The  $^{12}\text{CO}_2$  flux is enhanced by a factor of 2 to 4 over the complete range of the spectra. The  $^{13}\text{CO}_2$   $Q$ -branch however becomes more than an order of magnitude stronger, and the peak flux of the feature becomes higher than the peak flux of the neighbouring  $^{12}\text{CO}_2$  lines for the highest abundances. The spectra with enhanced  $\text{CO}_2$  abundances are shifted vertically for clarity.

$1 \times 10^{-6}$ ,  $1 \times 10^{-5}$ , and  $1 \times 10^{-4}$  around the  $\text{CO}_2$  iceline. The enhanced  $\text{CO}_2$  increases the  $^{12}\text{CO}_2$  flux up to a factor of 3. The optically thin  $^{13}\text{CO}_2$  feature is however increased by a lot more, with the peak flux in the  $^{13}\text{CO}_2$   $Q$ -branch reaching fluxes that are more than two times higher than peak fluxes of the nearby  $^{12}\text{CO}_2$   $P$ -branch lines.

Enhanced abundances in the outer regions can be distinguished from an enhanced abundance in the inner regions by looking at the tail of the  $^{13}\text{CO}_2$   $Q$ -branch. An over-abundant inner region will show a significant flux (10–50% of the peak) from the  $^{13}\text{CO}_2$   $Q$ -branch in the entire region between the locations of the  $^{12}\text{CO}_2$   $P(21)$  and  $P(23)$  lines and will show a smoothly declining profile with decreasing wavelength. If the abundance enhancement is in the outer regions, where the gas temperature and thus the rotational temperature is lower, the flux between the  $^{12}\text{CO}_2$   $P(21)$  and  $P(23)$  lines will be lower for the low enhancements (0–20% of the peak flux), for the higher enhancements the  $R(1)$  line shows up in the short wavelength side of the profile. Other  $R$  and  $P$  branch lines from  $^{13}\text{CO}_2$  can also show up in the spectrum if the abundance can reach up to  $10^{-4}$  in the ring around the  $\text{CO}_2$  iceline.

#### 4.3. Comparison of $\text{CO}_2$ with other inner disk molecules

With the models presented in this paper, four molecules with rovibrational transitions coming from the inner disk have been studied by non-LTE disk models:  $\text{H}_2\text{O}$  (Antonellini et al. 2015, 2016; Meijerink et al. 2009),  $\text{CO}$  (Thi et al. 2013),  $\text{HCN}$  (Bruderer et al. 2015) and  $\text{CO}_2$  (this work). Of these  $\text{CO}$  is special, as it can be excited by UV radiation and fluoresces to excited vibrational states that in turn emit infrared radiation. For the other molecules absorption of a UV photon mostly leads to dissociation of the molecule (Heays et al. 2017).  $\text{H}_2\text{O}$ ,  $\text{HCN}$  and  $\text{CO}$  all have an permanent dipole moment and can thus also emit strongly in the sub-millimeter. This means that these molecules will have lower rotational temperatures than  $\text{CO}_2$  in low density

gas but they are actually observed to have broader profiles in the mid-infrared. Thus, our models reinforce the conclusion from the observed profiles that  $\text{CO}_2$  comes from relatively cold gas (200–300 K; see panel c of Fig. 5 and panel d of Fig. C.1).

For the disk around AS 205 (N), the emission of both  $\text{HCN}$  and  $\text{CO}_2$  has now been analysed under non-LTE conditions in DALI. As such it is possible to infer the  $\text{HCN}$  to  $\text{CO}_2$  abundance ratio in the disk. The representative, constant abundance model for the  $\text{CO}_2$  emission from AS 205 N has an abundance of  $3 \times 10^{-8}$  with a gas-to-dust ratio of 1000 but the inner abundance can easily vary by an order of magnitude or more while still being in agreement with observations. The models from Bruderer et al. (2015) that best reproduce the data have outer  $\text{HCN}$  abundances between  $10^{-10}$  and  $10^{-9}$  for gas-to-dust ratios of 1000. This translates into  $\text{CO}_2/\text{HCN}$  abundance ratios of 30–300 in the region from 2 to 30 AU. The higher abundance of  $\text{CO}_2$  in the outer regions of the disk explains the colder inferred rotational temperature of  $\text{CO}_2$  compared to  $\text{HCN}$ .

## 5. Conclusion

Results of DALI models are presented, modelling the full continuum radiative transfer, non-LTE excitation of  $\text{CO}_2$  in a typical protoplanetary disk model, with as the main goal: to find a way to measure the  $\text{CO}_2$  abundance in the emitting region of disks with future instruments like JWST and test different assumptions on its origin. Spectra of  $\text{CO}_2$  and  $^{13}\text{CO}_2$  in the 4–4.5  $\mu\text{m}$  and 14–16  $\mu\text{m}$  regions were modelled for disks with different parametrized abundance structures, gas masses and dust masses. The main conclusions of this study are:

- The critical density of the  $\text{CO}_2$   $00^0_1$  state, responsible for emission around 4.3  $\mu\text{m}$ , is very high,  $>10^{15} \text{ cm}^{-3}$ . As a result, in the absence of a pumping radiation field, there is no emission from the  $00^0_1$  state at low densities. If there is a pumping infrared radiation field, or if the density is high

enough, the emission around 4.3  $\mu\text{m}$  will be brighter than that around 15  $\mu\text{m}$ .

- The infrared continuum radiation excites CO<sub>2</sub> up to large radii (10s of AU). The region probed by the CO<sub>2</sub> emission can therefore be an order of magnitude larger (in radius) than typically assumed in LTE slab models. Temperatures inferred from optically thin LTE models can also be larger than the actual temperature of the emitting gas. Differences between LTE and non-LTE full disk model flux are typically a within factor of three.
- Current observations of the 15  $\mu\text{m}$  Q-branch fluxes are consistent with models with constant abundances between 10<sup>-9</sup> and 10<sup>-7</sup> for a gas-to-dust ratio of 1000. Observations of lines corresponding to levels with high rotational quantum numbers or the <sup>13</sup>CO<sub>2</sub> Q-branch will have to be used to properly infer abundances. In particular, the <sup>13</sup>CO<sub>2</sub> Q-branch can be a good indicator of abundance structure from inner to outer disk.
- The gas-to-dust ratio and fractional abundance are largely degenerate. The column of CO<sub>2</sub> above the dust infrared photosphere sets the emission. Models with similar columns have very similar spectra irrespective of total dust and gas mass, due to the excitation mechanism of CO<sub>2</sub>. If the gas-to-dust ratio is constrained from other observations such as H<sub>2</sub>O the fractional abundance can be determined from the spectra.
- The abundance of CO<sub>2</sub> in protoplanetary disks inferred from modelling, 10<sup>-9</sup>–10<sup>-7</sup>, is at least two orders of magnitude lower than the CO<sub>2</sub> abundance in ISM ices. This implies that disk chemical abundances are not directly inherited from the ISM and that significant chemical processing happens between the giant molecular cloud stage and the protoplanetary disk stage.
- The <sup>13</sup>CO<sub>2</sub> v<sub>2</sub> Q-branch at 15.42  $\mu\text{m}$  will be able to identify an overabundance of CO<sub>2</sub> in the upper layers of the inner disk, such as could be produced by sublimating pebbles and planetesimals around the iceline(s).

Our work shows that the new instruments on JWST will be able to give a wealth of information on the CO<sub>2</sub> abundance structure, provided that high S/N (>300 on the continuum) spectra are obtained.

*Acknowledgements.* We thank the anonymous referee for his/her suggestions that have improved the paper. Astrochemistry in Leiden is supported by the European Union A-ERC grant 291141 CHEMPLAN, by the Netherlands Research School for Astronomy (NOVA), by a Royal Netherlands Academy of Arts and Sciences (KNAW) professor prize. This work is based in part on archival data obtained made with the *Spitzer* Space Telescope, which is operated by the Jet Propulsion Laboratory, California Institute of Technology under a contract with NASA.

## References

- Agúndez, M., Cernicharo, J., & Goicoechea, J. R. 2008, *A&A*, **483**, 831
- Alcalá, J. M., Natta, A., Manara, C. F., et al. 2014, *A&A*, **561**, A2
- Allen, D., Scragg, T., & Simpson, C. 1980, *Chem. Phys.*, **51**, 279
- Andrews, S. M., Wilner, D. J., Hughes, A. M., Qi, C., & Dullemond, C. P. 2009, *ApJ*, **700**, 1502
- Andrews, S. M., Rosenfeld, K. A., Kraus, A. L., & Wilner, D. J. 2013, *ApJ*, **771**, 129
- Antonellini, S., Kamp, I., Riviere-Marichalar, P., et al. 2015, *A&A*, **582**, A105
- Antonellini, S., Kamp, I., Lahuis, F., et al. 2016, *A&A*, **585**, A61
- Armitage, P. J. 2011, *ARA&A*, **49**, 195
- Banzatti, A., & Pontoppidan, K. M. 2015, *ApJ*, **809**, 167
- Banzatti, A., Pontoppidan, K. M., Salyk, C., et al. 2017, *ApJ*, **834**, 152
- Bast, J. E., Brown, J. M., Herczeg, G. J., van Dishoeck, E. F., & Pontoppidan, K. M. 2011, *A&A*, **527**, A119
- Bergin, E. A., Melnick, G. J., Gerakines, P. A., Neufeld, D. A., & Whittet, D. C. B. 2005, *ApJ*, **627**, L33
- Boogert, A. C. A., Gerakines, P. A., & Whittet, D. C. B. 2015, *ARA&A*, **53**, 541
- Boonman, A. M. S., van Dishoeck, E. F., Lahuis, F., & Doty, S. D. 2003a, *A&A*, **399**, 1063
- Boonman, A. M. S., van Dishoeck, E. F., Lahuis, F., et al. 2003b, *A&A*, **399**, 1047
- Brown, J. M., Pontoppidan, K. M., van Dishoeck, E. F., et al. 2013, *ApJ*, **770**, 94
- Bruderer, S. 2013, *A&A*, **559**, A46
- Bruderer, S., van Dishoeck, E. F., Doty, S. D., & Herczeg, G. J. 2012, *A&A*, **541**, A91
- Bruderer, S., Harsono, D., & van Dishoeck, E. F. 2015, *A&A*, **575**, A94
- Cami, J., Yamamura, I., de Jong, T., et al. 2000, *A&A*, **360**, 562
- Carr, J. S., & Najita, J. R. 2008, *Science*, **319**, 1504
- Carr, J. S., & Najita, J. R. 2011, *ApJ*, **733**, 102
- Chandra, S., & Sharma, A. K. 2001, *A&A*, **376**, 356
- Ciesla, F. J., & Cuzzi, J. N. 2006, *Icarus*, **181**, 178
- de Graauw, T., Whittet, D. C. B., Gerakines, P. A., et al. 1996, *A&A*, **315**, L345
- Draine, B. T., & Lee, H. M. 1984, *ApJ*, **285**, 89
- Drozovskaya, M. N., Walsh, C., van Dishoeck, E. F., et al. 2016, *MNRAS*, **462**, 977
- Eistrup, C., Walsh, C., & van Dishoeck, E. F. 2016, *A&A*, **595**, A83
- Faure, A., & Josselin, E. 2008, *A&A*, **492**, 257
- Fedele, D., Pascucci, I., Brittain, S., et al. 2011, *ApJ*, **732**, 106
- Gibb, E. L., & Horne, D. 2013, *ApJ*, **776**, L28
- Gibb, E. L., Whittet, D. C. B., Boogert, A. C. A., & Tielens, A. G. G. M. 2004, *ApJS*, **151**, 35
- Gibb, E. L., Van Brunt, K. A., Brittain, S. D., & Rettig, T. W. 2007, *ApJ*, **660**, 1572
- González-Alfonso, E., & Cernicharo, J. 1999, in *The Universe as Seen by ISO*, eds. P. Cox & M. Kessler, ESA SP, 427, 325
- Harsono, D., Bruderer, S., & van Dishoeck, E. F. 2015, *A&A*, **582**, A41
- Heays, A. N., Bosman, A. D., & van Dishoeck, E. F. 2017, *A&A*, in press, DOI: 10.1051/0004-6361/201628742
- Henning, T., & Semenov, D. 2013, *Chem. Rev.*, **113**, 9016
- Horne, K., & Marsh, T. R. 1986, *MNRAS*, **218**, 761
- Jacobs, R. R., Pettipiece, K. J., & Thomas, S. J. 1975, *Phys. Rev. A*, **11**, 54
- Jacquinet-Husson, N., Crepeau, L., Armante, R., et al. 2011, *J. Quant. Spectr. Rad. Transf.*, **112**, 2395
- Jones, A., Noll, S., Kausch, W., Szyszka, C., & Kimeswenger, S. 2013, *A&A*, **560**, A91
- Lahuis, F., van Dishoeck, E. F., Boogert, A. C. A., et al. 2006, *ApJ*, **636**, L145
- Lambrechts, M., & Johansen, A. 2012, *A&A*, **544**, A32
- Le Roy, L., Altwegg, K., Balsiger, H., et al. 2015, *A&A*, **583**, A1
- Levison, H. F., Kretke, K. A., & Duncan, M. J. 2015, *Nature*, **524**, 322
- Madhusudhan, N., Knutson, H., Fortney, J. J., & Barman, T. 2014, in *Protostars and Planets VI*, eds. H. Beuther, R. Klessen, C. Dullemond, & T. Henning (Tucson: Universit of Arizona Press), 739
- Manara, C. F., Fedele, D., Herczeg, G. J., & Teixeira, P. S. 2016, *A&A*, **585**, A136
- Mandell, A. M., Bast, J., van Dishoeck, E. F., et al. 2012, *ApJ*, **747**, 92
- Markwick, A. J., Ilgner, M., Millar, T. J., & Henning, T. 2002, *A&A*, **385**, 632
- Meijerink, R., Pontoppidan, K. M., Blake, G. A., Poelman, D. R., & Dullemond, C. P. 2009, *ApJ*, **704**, 1471
- Milam, S. N., Savage, C., Brewster, M. A., Ziurys, L. M., & Wyckoff, S. 2005, *ApJ*, **634**, 1126
- Mumma, M. J., & Charnley, S. B. 2011, *ARA&A*, **49**, 471
- Najita, J., Carr, J. S., & Mathieu, R. D. 2003, *ApJ*, **589**, 931
- Najita, J. R., Ádámkóvics, M., & Glassgold, A. E. 2011, *ApJ*, **743**, 147
- Neufeld, D. A. 2012, *ApJ*, **749**, 125
- Nevdakh, V., Orlov, L., & Leshenyuk, N. 2003, *J. Appl. Spectr.*, **70**, 276
- Noll, S., Kausch, W., Barden, M., et al. 2012, *A&A*, **543**, A92
- Öberg, K. I., Boogert, A. C. A., Pontoppidan, K. M., et al. 2011, *ApJ*, **740**, 109
- Ormel, C. W., & Klahr, H. H. 2010, *A&A*, **520**, A43
- Pascucci, I., Apai, D., Luhman, K., et al. 2009, *ApJ*, **696**, 143
- Pascucci, I., Herczeg, G., Carr, J. S., & Bruderer, S. 2013, *ApJ*, **779**, 178
- Pontoppidan, K. M. 2016, CHIP: Caltech High-res IRS Pipeline, Astrophysics Source Code Library [record ascl: 1602.017]
- Pontoppidan, K. M., & Blevins, S. M. 2014, *Faraday Discussions*, **169**, 49
- Pontoppidan, K. M., Boogert, A. C. A., Fraser, H. J., et al. 2008, *ApJ*, **678**, 1005
- Pontoppidan, K. M., Meijerink, R., Dullemond, C. P., & Blake, G. A. 2009, *ApJ*, **704**, 1482
- Pontoppidan, K. M., Salyk, C., Blake, G. A., et al. 2010, *ApJ*, **720**, 887
- Pontoppidan, K. M., Blake, G. A., & Smette, A. 2011, *ApJ*, **733**, 84
- Procaccia, I., & Levine, R. D. 1975, *J. Chem. Phys.*, **63**, 4261

- Rieke, G. H., Wright, G. S., Böker, T., et al. 2015, *PASP*, **127**, 584
- Rigliaco, E., Pascucci, I., Duchene, G., et al. 2015, *ApJ*, **801**, 31
- Rothman, L., Gordon, I., Babikov, Y., et al. 2013, *J. Quant. Spectr. Radiat. Transf.*, **130**, 4
- Rothman, L., Gordon, I., Barbe, A., et al. 2009, *J. Quant. Spectr. Radiat. Transf.*, **110**, 533
- Salyk, C., Pontoppidan, K. M., Blake, G. A., et al. 2008, *ApJ*, **676**, L49
- Salyk, C., Blake, G. A., Boogert, A. C. A., & Brown, J. M. 2011a, *ApJ*, **743**, 112
- Salyk, C., Pontoppidan, K. M., Blake, G. A., Najita, J. R., & Carr, J. S. 2011b, *ApJ*, **731**, 130
- Schöier, F. L., van der Tak, F. F. S., van Dishoeck, E. F., & Black, J. H. 2005, *A&A*, **432**, 369
- Stevenson, D. J., & Lunine, J. I. 1988, *Icarus*, **75**, 146
- Tashkun, S., Perevalov, V., Gamache, R., & Lamouroux, J. 2015, *J. Quant. Spectr. Rad. Transf.*, **152**, 45
- Taylor, R. L., & Bitterman, S. 1969, *Rev. Mod. Phys.*, **41**, 26
- Thi, W. F., Kamp, I., Woitke, P., et al. 2013, *A&A*, **551**, A49
- Udry, S., & Santos, N. C. 2007, *ARA&A*, **45**, 397
- van der Plas, G., van den Ancker, M. E., Fedele, D., et al. 2008, *A&A*, **485**, 487
- van der Tak, F. F. S., Black, J. H., Schöier, F. L., Jansen, D. J., & van Dishoeck, E. F. 2007, *A&A*, **468**, 627
- van Dishoeck, E. F., Helmich, F. P., de Graauw, T., et al. 1996, *A&A*, **315**, L349
- Walsh, C., Millar, T. J., Nomura, H., et al. 2014, *A&A*, **563**, A33
- Walsh, C., Nomura, H., & van Dishoeck, E. 2015, *A&A*, **582**, A88
- Weingartner, J. C., & Draine, B. T. 2001, *ApJ*, **548**, 296
- Wells, M., Pel, J.-W., Glasse, A., et al. 2015, *PASP*, **127**, 646
- Willacy, K., Klahr, H. H., Millar, T. J., & Henning, T. 1998, *A&A*, **338**, 995
- Wilson, T. L., & Rood, R. 1994, *ARA&A*, **32**, 191
- Winn, J. N., & Fabrycky, D. C. 2015, *ARA&A*, **53**, 409
- Winston, E., Megeath, S. T., Wolk, S. J., et al. 2010, *AJ*, **140**, 266
- Woitke, P., Kamp, I., & Thi, W.-F. 2009, *A&A*, **501**, 383
- Yang, B., Stancil, P. C., Balakrishnan, N., & Forrey, R. C. 2010, *ApJ*, **718**, 1062

**Table A.1.** Vibrational rate coefficients as measured/extrapolated.

Initial state	Final state	Rate Coef. [cm <sup>3</sup> s <sup>-1</sup> ]
01 <sup>1</sup> 0	00 <sup>0</sup> 0	5(-12)
10 <sup>0</sup> 0(2)	00 <sup>0</sup> 0	3.3(-12)
10 <sup>0</sup> 0(2)	01 <sup>1</sup> 0	1(-11)
02 <sup>2</sup> 0	00 <sup>0</sup> 0	3.3(-12)
02 <sup>2</sup> 0	01 <sup>1</sup> 0	1(-11)
02 <sup>2</sup> 0	10 <sup>0</sup> 0(2)	5.8(-12)
10 <sup>0</sup> 0(1)	00 <sup>0</sup> 0	3.3(-12)
10 <sup>0</sup> 0(1)	01 <sup>1</sup> 0	1(-11)
10 <sup>0</sup> 0(1)	10 <sup>0</sup> 0(2), 02 <sup>2</sup> 0	5.8(-12)
11 <sup>1</sup> 0(2)	00 <sup>0</sup> 0(1)	3(-12)
11 <sup>1</sup> 0(2)	01 <sup>1</sup> 0(1)	9(-12)
11 <sup>1</sup> 0(2)	10 <sup>0</sup> 0(1, 2), 02 <sup>2</sup> 0	1.5(-11)
03 <sup>3</sup> 0	00 <sup>0</sup> 0	3(-12)
03 <sup>3</sup> 0	01 <sup>1</sup> 0	9(-12)
03 <sup>3</sup> 0	10 <sup>0</sup> 0(1, 2), 02 <sup>2</sup> 0	1.5(-11)
03 <sup>3</sup> 0	11 <sup>1</sup> 0(2)	5.8(-12)
11 <sup>1</sup> 0(1)	00 <sup>0</sup> 0	3(-12)
11 <sup>1</sup> 0(1)	01 <sup>1</sup> 0	9(-12)
11 <sup>1</sup> 0(1)	10 <sup>0</sup> 0(1, 2), 02 <sup>2</sup> 0	1.5(-11)
11 <sup>1</sup> 0(1)	11 <sup>1</sup> 0(2), 03 <sup>3</sup> 0	5.8(-12)
00 <sup>0</sup> 1	11 <sup>1</sup> 0(1, 2), 03 <sup>3</sup> 0	4.5(-14)
01 <sup>1</sup> 1	11 <sup>1</sup> 0(1, 2), 03 <sup>3</sup> 0	4.5(-14)
01 <sup>1</sup> 1	00 <sup>0</sup> 1	5(-12)

Notes.  $a(b) = a \times 10^b$ .

## Appendix A: Collisional rate coefficients

The collisional rate coefficients are calculated in a way very similar to [Bruderer et al. \(2015\)](#), that is by combining vibrational coefficients with rotational rate coefficients to get the state-to-state ro-vibrational rate coefficients. Only collisions with H<sub>2</sub> are considered, which is the dominant gas species in the regions where CO<sub>2</sub> is expected to be abundant. The vibrational coefficients were taken from the laser physics and atmospheric physics papers. An overview of the final vibrational rate coefficients used are shown in [Table A.1](#). The temperature dependence of the rates is suppressed for the de-excitation collisional rate coefficients and the rate for 300 K are used throughout. The vibrational rate coefficients are not expected to vary much over the range of temperatures considered here. The de-excitation rate coefficient of the bending mode by H<sub>2</sub> (01<sup>1</sup>0 → 00<sup>0</sup>0 transition) from [Allen et al. \(1980\)](#) is  $5 \times 10^{-12}$  cm<sup>3</sup> s<sup>-1</sup>, an order of magnitude faster than the He ([Taylor & Bitterman 1969](#); [Allen et al. 1980](#)). This is probably due to vibrational-rotational energy exchange in collisions with rotationally excited H<sub>2</sub> ([Allen et al. 1980](#)). For levels higher up in the vibrational ladder we extrapolate the rates as in [Procaccia & Levine \(1975\)](#) and [Chandra & Sharma \(2001\)](#). Combining Eqs. (6) and (8) from the later paper we get, for  $v > w$ , the relation

$$k(v_2 = v \rightarrow v_2 = w) = v \frac{2w + 1}{2v + 1} k(v_2 = 1 \rightarrow v_2 = 0). \quad (\text{A.1})$$

The rate coefficient measured by [Nevdakh et al. \(2003\)](#) is actually the total quenching rate of the 00<sup>0</sup>1 level. Here we assume that the relaxation of the 00<sup>0</sup>1 level goes to the three closest

lower energy levels (03<sup>3</sup>0, 11<sup>1</sup>0(1), 11<sup>1</sup>0(2)) in equal measure. For all the rates between the levels of the Fermi degenerate states and the corresponding bending mode with higher angular momentum the CO<sub>2</sub>-CO<sub>2</sub> rate measured by [Jacobs et al. \(1975\)](#) was used scaled to the reduced mass of the H<sub>2</sub>-CO<sub>2</sub> system. The states with constant  $2v_1 + v_2$  are considered equal to the pure bending mode with respect to the collisional rate coefficients to other levels.

No information exists on the rotational rate coefficients of CO<sub>2</sub> with H<sub>2</sub>. We have decided to use the CO rate coefficients from [Yang et al. \(2010\)](#) instead. Since CO<sub>2</sub> does not have a dipole moment, the exact rate coefficients are not expected to be important since the critical densities for the levels in the rotational ladders are very low,  $< 10^4$  cm<sup>-3</sup>.

The method suggested by [Faure & Josselin \(2008\)](#) was employed to calculate the state-to-state de-excitation rate coefficients for initial levels  $v, J$  to all levels  $v', J'$  with a smaller ro-vibrational energy. This is assuming a decoupling of rotational and vibrational levels, so we can write

$$k(v, J \rightarrow v', J'; T) = k(v \rightarrow v') \times P_{(J, J')}(T), \quad (\text{A.2})$$

where

$$P_{(J, J')}(T) = \frac{k(0, J \rightarrow 0, J'; T) \sum_J g_J \exp(-E_{v, J}/kT)}{\sum_J g_J \exp(-E_{v, J}/kT) \sum_{J'} k(0, J \rightarrow 0, J'; T)}, \quad (\text{A.3})$$

with the statistical weights  $g_i$  of the levels. All the excitation rates are calculated using the detailed balance.

## Appendix B: Fast line ray tracer

For the calculation of the CO<sub>2</sub> lines a new ray tracer was used. The conventional ray tracer used in DALI ([Bruderer et al. 2012](#)) can take up to ten minutes to calculate the flux from one line. The CO<sub>2</sub> molecule model used here includes more than 3600 lines. Not all of these lines are directly important but to get the complete spectrum of both the 4.3 μm and the 15 μm bands, a few hundred lines need to be ray traced for each model.

To enable the calculation of a large number of lines a module has been implemented into DALI that can calculate a line flux in a few seconds versus a few minutes for the conventional ray tracer. The module uses the fact that, along a line of sight, the velocity shear due to the finite height of the disk is approximately linear ([Horne & Marsh 1986](#), Eqs. (9) and (10)). Using this, the spectrum for an annulus in the disk can be approximated. At the radius of the annulus in question, the spectra are calculated for different velocity shears. These spectra are calculated by vertically integrating the equation of radiative transfer through the disk and correcting for the projected area for non face-on viewing angles. Then the total spectrum of the annulus is calculated by iterating over the azimuthal direction. For each angle the velocity shear is calculated and the spectrum is interpolated from the pre-calculated spectra. A simple sum over the spectra in all annuli is now sufficient to calculate the total spectrum.

This approximation is a powerful tool for calculating the total flux in a line especially for low inclinations. For the models presented in this paper the fluxes differ by about 4% for the 15 μm lines and 1.5% for the 4.3 μm lines. This is small compared to the other uncertainties in the models.

The approximation breaks down at high inclinations and should be used with care for any inclination larger than 45°. The total line shape is also close to the line shape from the traditional ray tracer, but with the high S/N from ALMA, using the traditional ray tracer is still advised for doing direct comparisons.

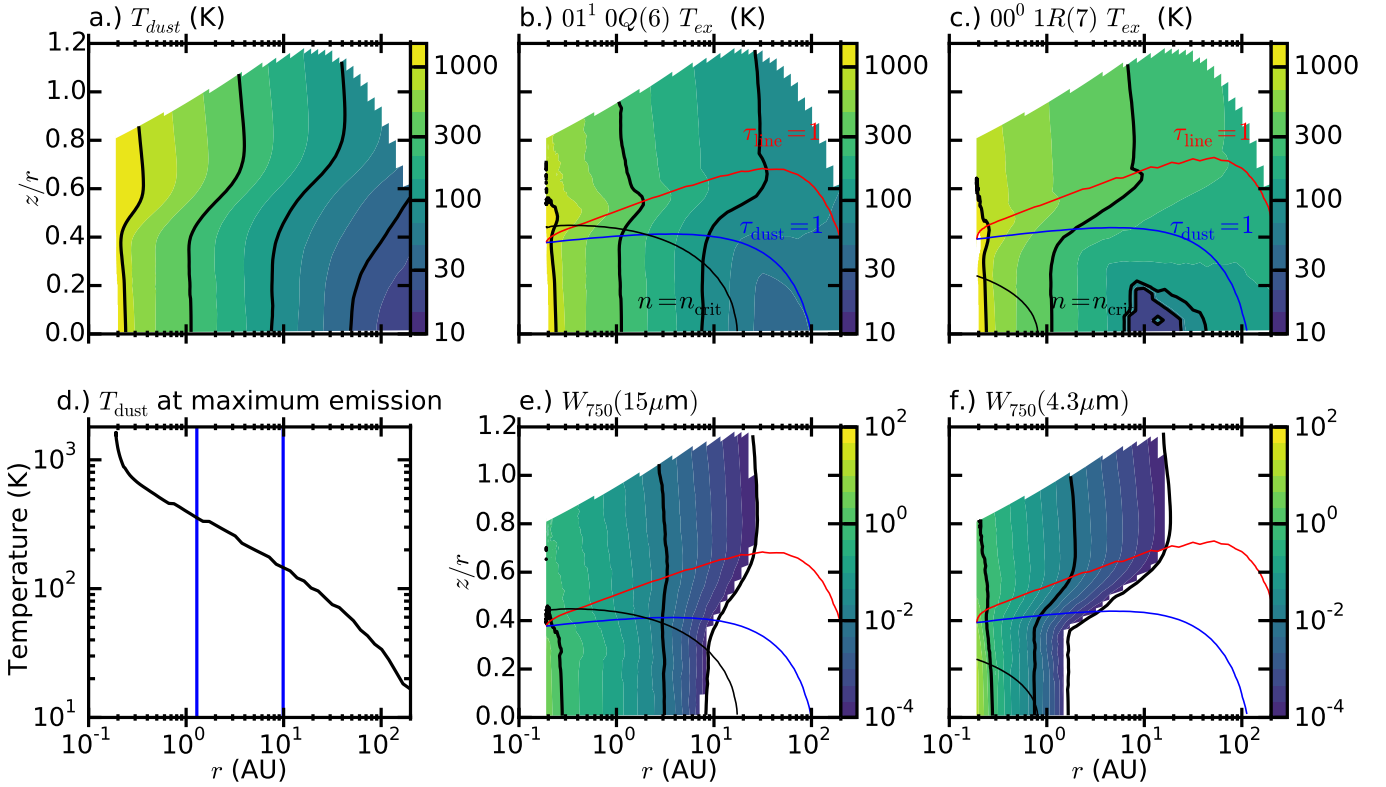


**Fig. C.1.** Dust temperature, excitation temperature and radiation field for a model with  $g/d_{\text{gas}} = 1000$ , and a constant abundance of  $10^{-7}$ . The red line in panels **b**), **c**), **e**) and **f**) shows the  $\text{CO}_2$  line  $\tau = 1$  surface, the blue line shows the  $\tau = 1$  line for the dust. Panel **d**) shows the dust temperature at the height from which most of the emission of the  $15 \mu\text{m}$   $Q(6)$  line originates as function of radius. The vertical blue lines enclose the radii that account for 50% of the emission.

This is also the case for images for which the errors will be larger than for the integrated flux or line shape as some of the errors made in making the image will cancel out (in first order) when integrating over the annulus.

### Appendix C: Model temperature and radiation structure

Figure C.1 shows the model temperature, radiation field and excitation temperature structure corresponding to the model shown in Fig. 5. Panel a shows the dust temperature structure, panels b and c show the excitation temperature of the  $v_2 1 \rightarrow 0 Q(6)$  line and  $v_3 1 \rightarrow 0 R(7)$  lines. For the excitation temperature only the upper and lower state of the line are used. This is thus a vibrational excitation temperature and can be different from the ground state rotational excitation temperature (that follows the dust temperature) and the rotational excitation temperature within a vibrationally excited state. Where the density is higher than the critical density the excitation temperature is equal to the dust temperature. In the disk atmosphere the  $Q(6)$  is mostly subthermally excited, while the  $R(7)$  line is superthermally excited. For both lines there is a maximum in the vertical excitation temperature distribution at the point where the gas becomes optically thick to its own radiation. Panel d shows the dust temperature of the region from which most of the  $\text{CO}_2$   $15 \mu\text{m}$  emission originates as function of radius. Most of the emitting gas is at temperatures between 150 and 350 K. Panels e and f show the strength of the radiation field at  $15 \mu\text{m}$  and  $4.3 \mu\text{m}$  is shown as a factor of the radiation field of a 750 K blackbody. This shows where there is a sufficient photon density to radiatively pump  $\text{CO}_2$ .

### Appendix D: Model fluxes $g/d_{\text{dust}}$

As mentioned in the main text, two different way of changing the gas-to-dust ratio were considered, increasing the gas mass and decreasing the dust mass w.r.t. the gas-to-dust ratio 100 case. Figure D.1 is the counterpart to Fig. 6 showing the modelled fluxes for different inner  $\text{CO}_2$  abundances, outer  $\text{CO}_2$  abundances and different gas-to-dust ratios. In this case the gas-to-dust ratio is varied by keeping the gas mass of the disk constant and decreasing the amount of dust in the disk.

There are only very slight differences between Figs. D.1 and 6, and all observations made for the figure in the main text are true for this figure as well.

### Appendix E: LTE vs. non-LTE

The effects of the LTE assumption on the line fluxes in a full disk model on the  $v_3, 1 \rightarrow 0, R(7)$  line and the  $15 \mu\text{m}$  feature are shown in Fig. E.1. Only the models with constant ( $x_{\text{out}} = x_{\text{in}}$ ) are shown for clarity but the differences between LTE and non-LTE for these models are representative for the complete set of models. For the  $15 \mu\text{m}$  flux the differences between the LTE and non-LTE models is small, of the order of 30%. The radial extent of the emission is, however, different: the region emitting 75% of the  $15 \mu\text{m}$  flux extends twice as far in the non-LTE models (extent of the  $15 \mu\text{m}$  non-LTE emission is seen in Fig. 5, panel f). This a clear sign of the importance of infrared pumping that is included in the non-LTE models. The difference between the fluxes in the  $4.25 \mu\text{m}$  line are greater, up to an order of magnitude. The difference are strongest in the models that have a low total  $\text{CO}_2$  content (so low abundance

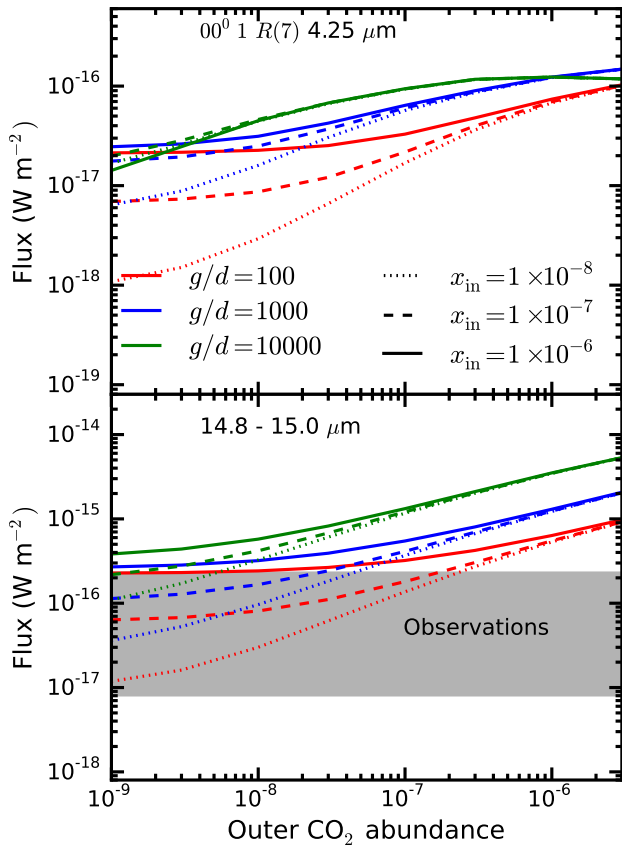


**Fig. D.1.** Line fluxes for models with constant gas mass ( $g/d_{\text{dust}}$ ). The upper panel shows the flux of the  $R(7)$  line from the fundamental asymmetric stretch band at  $4.25 \mu\text{m}$ . The lower panel shows the flux contained in the  $15 \mu\text{m}$  feature. The grey region denotes the range in line fluxes as observed by Salyk et al. (2011b) scale to the distance of AS 205 N. This feature contains the flux from multiple  $Q$ -branches with  $\Delta v_2 = 1$ . The CO<sub>2</sub> flux depends primarily on the outer CO<sub>2</sub> abundance and the total  $g/d$  ratio and does not strongly depend on the inner CO<sub>2</sub> abundances. Only for the very low CO<sub>2</sub> absolute abundances in the outer regions is the effect of the inner abundance on the line fluxes visible.

and low gas-to-dust ratio). This is mostly due to the larger radial extent of the emitting region extending up to 20 times further out in the non-LTE models compared to the corresponding LTE model (Extent of the  $4.3 \mu\text{m}$  non-LTE emission is seen in Fig. 5, panel i). This is in line with the higher Einstein A coefficient and upper level energy (and thus higher critical density) of the  $v_3, 1 \rightarrow 0, R(7)$  line, giving rise to a large importance of infrared pumping relative to collisional excitation. Figure E.1 uses  $g/d_{\text{dust}} = 1000$ , but the plot for  $g/d_{\text{gas}} = 1000$  is very similar.

## Appendix F: Line blending by H<sub>2</sub>O and OH

One of the major challenges in interpreting IR-spectra of molecules in T Tauri disks are the ubiquitous water lines. H<sub>2</sub>O has a large dipole moment and thus has strong transitions. As H<sub>2</sub>O chemically favours hot regions (Agúndez et al. 2008; Walsh et al. 2015) there are a lot of rotational lines in the mid infra-red. Figure F.1 shows the H<sub>2</sub>O rotational lines near the CO<sub>2</sub>  $15 \mu\text{m}$  feature. The spectra are simulated with a LTE slab model using the same parameters as fitted by Salyk et al. (2011b) for

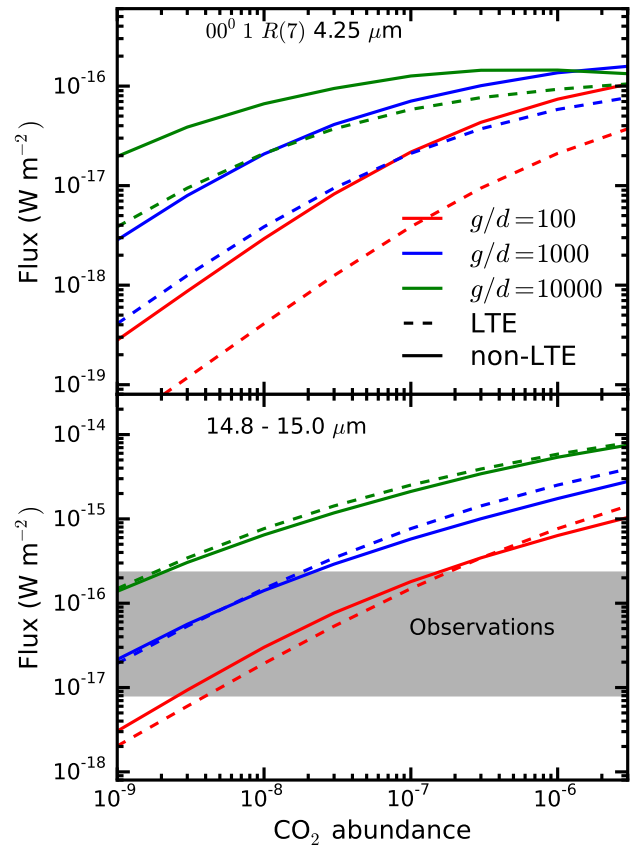


**Fig. E.1.** Flux comparison between LTE and non-LTE models. The upper panels show the flux of the  $R(7)$  line from the fundamental asymmetric stretch band. The lower panels show the flux contained in the  $15 \mu\text{m}$  feature. The grey region shows the range of observed flux by Salyk et al. (2011b). The abundance in these models is constant over the whole disk. For the  $15 \mu\text{m}$  feature the flux differences are small of the order of 30%. The differences are more pronounced in the  $4.25 \mu\text{m}$  flux where the differences can get as large as a factor of 4.

**Table F.1.** Parameters for the slab models.

Molecule	Column ( $\text{cm}^{-2}$ )	Temperature (K)
CO <sub>2</sub>	$4 \times 10^{15}$	300
H <sub>2</sub> O	$4 \times 10^{20}$	300
OH	$6 \times 10^{16}$	700

AS 205 (N) as reproduced in Table F.1. It should be noted that AS 205 (N) is a very water rich disk (in its spectra) explaining the large number of strong lines. Fortunately, there are still some regions in the CO<sub>2</sub> spectrum that are not blended with H<sub>2</sub>O or OH lines and thus can be used for tracing the CO<sub>2</sub> abundance structure independent of a H<sub>2</sub>O emission model. The situation improves at higher resolving power as can be seen in Fig. F.2. The resolving power of 28000 has been chosen to match with the resolving power of the SPICA HRS mode. At this point the line widths are dominated by the assumed Keplerian linewidth of  $20 \text{ km s}^{-1}$ . At this resolution the individual  $Q$ -branch lines are separable and a lot of the line blends that happen at a resolving power of 2200 are no longer an issue.

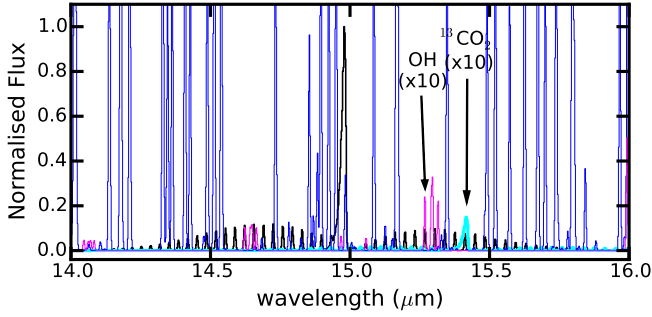


**Fig. F.1.** Slab model spectrum comparing CO<sub>2</sub> emission (black) and <sup>13</sup>CO<sub>2</sub> emission (cyan) with the H<sub>2</sub>O emission (blue) and OH emission (magenta) at a resolving power of 2200. Slab models uses the parameters fitted by Salyk et al. (2011b) for AS 205 (N) (see Table F.1). The large number of strong water lines strongly contaminates the CO<sub>2</sub> spectrum. All spectra are normalized to the peak of the CO<sub>2</sub> emission. A lot of single water lines are up to four times as strong as the peak of the CO<sub>2</sub> 15 μm feature. The <sup>13</sup>CO<sub>2</sub> and OH fluxes have been multiplied by a factor of 10 for clarity.

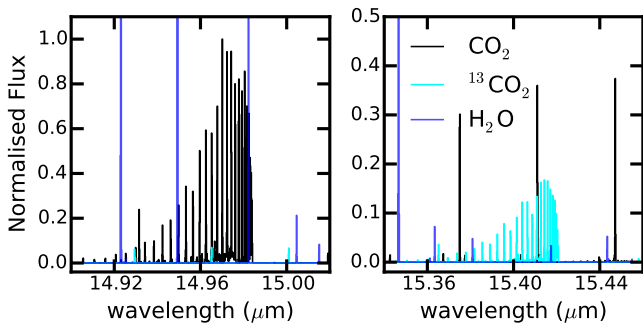


**Fig. F.2.** Slab model spectrum comparing CO<sub>2</sub> emission (black) and <sup>13</sup>CO<sub>2</sub> emission (cyan) with the H<sub>2</sub>O emission (blue) at a resolving power of 28 000. The left panel shows a zoom of the 15 μm region, the right panel shows a zoom in of the region where the <sup>13</sup>CO<sub>2</sub> v<sub>2</sub> Q-branch resides. Slab models uses the parameters fitted by Salyk et al. (2011b) for AS 205 (N) (see Table F.1). Due to the high resolving power individual Q-branch lines can be observed and blends are less likely to happen. A Keplerian linewidth of 20 km s<sup>-1</sup> has been assumed. The <sup>13</sup>CO<sub>2</sub> fluxes have been multiplied by a factor of 10 for clarity.

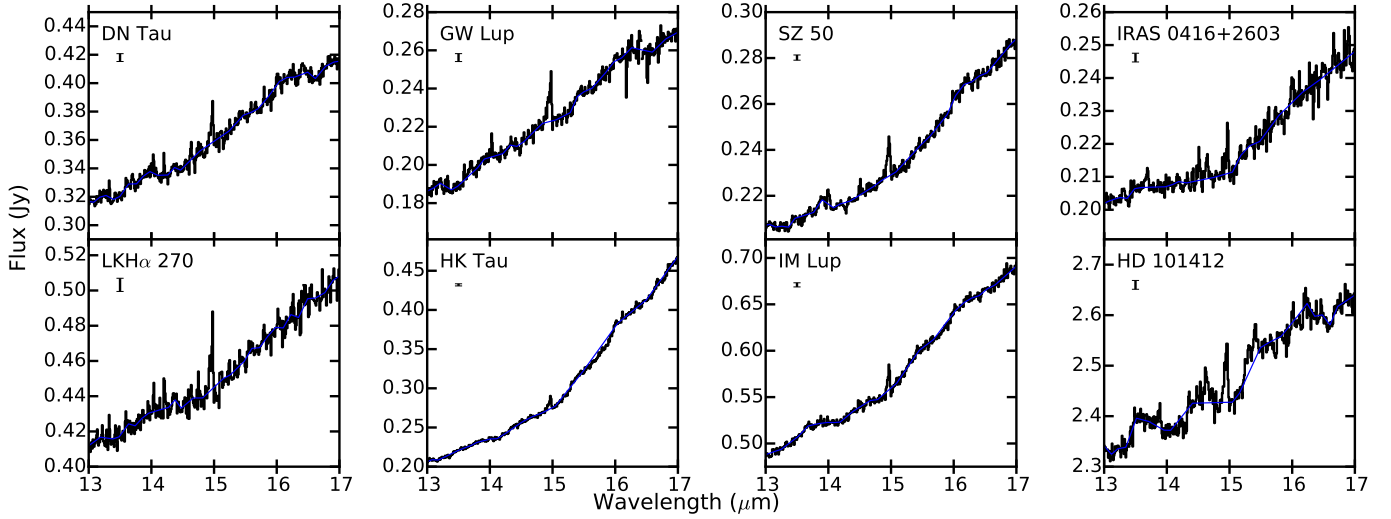
**Table G.1.** Stellar parameters.

Object	Source luminosity ( $L_{\odot}$ )	Distance (pc)	References
AS 205 N	7.3	125	Andrews et al. (2009)
DR Tau	1.0	140	Rigliaco et al. (2015)
DoAr24E	11	125	Rigliaco et al. (2015)
RNO 90	2.7	125	Rigliaco et al. (2015)

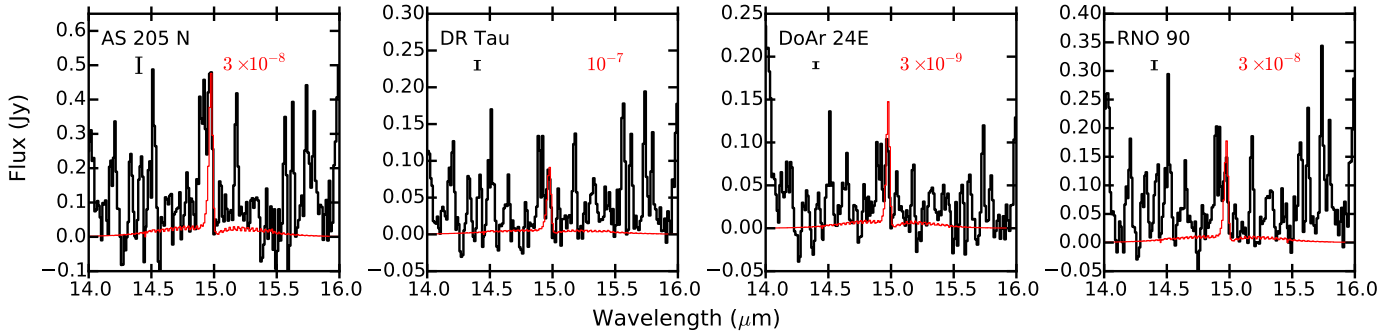
## Appendix G: *Spitzer*-IRS spectra

Figure G.1 shows the spectra as observed by *Spitzer*-IRS reduced with the CHIP software (Pontoppidan et al. 2010; Pontoppidan 2016). Continua that have been fitted to these spectra are also indicated on the figure. The objects have been chosen because their spectra are relatively free of H<sub>2</sub>O emission. Even without H<sub>2</sub>O lines, it is still tricky to determine a good baseline for the continuum as there are a lot of spectral slope changes, even in the narrow wavelength range considered here. This is especially true for HD 101412 where the full spectrum shows a hint of what looks like *R*- and *P*-branches. If these are features due to line emission, it becomes arbitrary where one puts the actual continuum, thus these features are counted here as part of the continuum. Whether these feature are real or not will not matter a lot for the abundance determination as the CO<sub>2</sub> *Q*-branch is separated from the strong *R*- and *P*-branch lines.

Figure G.2 shows a comparison between observed spectra of disk with strong H<sub>2</sub>O emission and CO<sub>2</sub> model spectra. The spectra are corrected for source luminosity and distance as explained in Sect. 4.1. Assumed distances and luminosities are given in Table G.1.



**Fig. G.1.** Observations from *Spitzer*-IRS over 13–17  $\mu\text{m}$  (black) with continuum as fitted (blue) for the eight selected sources. Typical rms noise on the continuum is shown under the object name. DN Tau, GW Lup and LKH $\alpha$  270 had a spike in the observed flux at 16.48  $\mu\text{m}$  due to artefacts at the edge of the observing order. This single data point has been removed from these three spectra.



**Fig. G.2.** Comparison of continuum subtracted *Spitzer* observations with luminosity and distance corrected model spectra for CO<sub>2</sub>. Object name and median rms noise in the spectra are given in the upper left corner of each panel. All of the sources here have strong H<sub>2</sub>O emission.